Published in final edited form as:
Anal Chem. 2012 January 17; 84(2): 793–821. doi:10.1021/ac2029024.

High-Q Optical Sensors for Chemical and Biological Analysis

Matthew S. Luchansky and **Ryan C. Bailey***
Department of Chemistry, University of Illinois at Urbana-Champaign, 600 S. Mathews Ave., Urbana, IL 61801

Introduction

Optical sensors represent a vitally important class of analytical tools that have been used to provide chemical information ranging from analyte concentration and binding kinetics to microscopic imaging and molecular structure. Optical sensors utilize a variety of signal transduction pathways based on photonic attributes that include absorbance, transmission, fluorescence intensity, refractive index, polarization, and reflectivity. Within the broad classification of optical sensors, refractive index (RI) sensors, which include devices such as surface plasmon resonance instruments, interferometers, diffraction gratings, optical fibers, photonic crystals, and resonant microcavities, have emerged as promising technologies over the past two decades. These optical sensors based on the change in RI associated with analyte binding involve an impressive array of instrumentation that allows for label-free[1] molecular sensing without the added complexity of fluorescent or enzymatic tags. By removing the requirement for labels, RI-based sensing allows for real-time and direct detection of molecular interactions at a dielectric interface. Though many manifestations of RI-based sensors have been proposed and demonstrated, high-quality factor (high-Q) optical sensors based on multi-pass photonic microstructures have recently emerged as an extremely promising, and perhaps the most sensitive, class of label-free sensors. Major advantages of many high-Q sensors include multiple-pass interactions between the propagating electromagnetic radiation and the respective analyte binding event, as well as the intrinsic chip-integration and wafer-scale fabrication that accompany many semiconductor-based sensing modalities.

High-Q optical sensors involve microstructures that confine light due to differences in RI between a micropatterned material and its surrounding. This confinement supports multi-pass light interactions based on either multiple reflections or many circumnavigations. In both cases, this results in an increased effective optical path length that improves the sensitivity of the device. The Q factor of a given device is a measure of the resonant photon lifetime within a microstructure (higher Q factor = longer lifetime), and therefore Q is directly correlated to the number of times a photon is recirculated and allowed to interact with the analyte.[2] Light is confined by either total internal reflection at a core/cladding interface (microcavities) or by the spatially periodic modulation of materials with different RI properties (photonic crystals), and resultant high-Q sensors interact with their local environments via an evanescent optical field that extends from the sensor surface and decays exponentially with distance.[3, 4] A more detailed treatment of microcavity technology involving whispering gallery mode (WGM) sensing will be presented in the following section. High-Q optical sensors, whether based on guided-mode optics or photonic crystal (PC) structures, support resonances at very specific wavelengths, and these resonances are responsive to changes in the effective RI at the device surface. For most microcavity

*Corresponding Author: Ryan C. Bailey, baileyrc@illinois.edu, 44 Roger Adams Lab, 600 South Mathews Avenue, Urbana, IL, 61801, (217) 333-0676.

sensors, the wavelengths of light transmitted between an adjacent waveguide or optical fiber and the cavity is attenuated at narrow resonant wavelengths that are a function of the RI at the microcavity surface; for most PC sensors, light is back-reflected only at precise resonance wavelengths. As the Q factor of a device increases, the photon lifetime increases, and the resonance wavelength peak becomes narrower. For both microcavity and PC sensors, the relative shift in resonance wavelengths is directly proportional to the effective RI sampled by the confined optical mode, which samples the dielectric interface via the evanescent wave extending from the sensor surface. Since most analytes, such as organic (bio)molecules in water or gases in air, have a greater dielectric permittivity (and thus higher RI) than the surrounding medium, their binding or association with the sensor surface leads to an increase in effective RI sampled by the optical mode.[4] Though factors such as biological and spectroscopic noise often set the practical limit of detection for any sensor system, the narrow resonance wavelengths associated with high-Q cavities provide an opportunity to resolve tiny spectral shifts that accompany a very small number of analyte binding interactions. The impressive sensitivity of microcavity and PC devices to minute changes in the effective RI at the sensor surface is the basis for most of the recent applications of high-Q optical sensors.

The development of high-Q photonic devices has been tremendously enabled by recent advances in micro- and nanofabrication methods, and the application of these devices for chemical and biomolecular analysis has only come to fruition within the past decade. This review focuses on the most exciting research in this area over the period of 2009–2011, although enabling findings and developments that precede this range are also covered. Recent reviews have summarized advances that may include some treatment of high-Q sensors, but these reviews have been broadly focused on advances in label-free sensors in general,[5–8] on applications of silicon photonics that include sensing among many others,[9] or on a general treatment of optical devices for sensing that includes the devices of interest.[10–13] Other excellent reviews are more narrowly focused and cover different aspects of high-Q technology, focusing specifically on ring resonator technology,[14, 15] microsphere resonators,[16] photonic crystals,[4, 17] microfluidic integration with optical sensors,[18, 19] and high-Q mechanical sensors.[20] This review considers recent advances in high-Q and ultra-high-Q optical sensors for addressing fundamental challenges in measurement science, giving special attention to those techniques that demonstrate useful chemical or biomolecular measurement capabilities within relevant real-world matrices. Although not rigorously fitting within some strict definitions of high-Q devices, photonic crystal sensors are covered as they represent an exciting complementary technology that, in many ways, is more advanced at present than many high-Q microcavity sensor configurations. As this review is intended to target the broad community of practicing analytical chemists, particular focus is given to signal transduction mechanisms, surface chemistry, assay methodologies, and interesting new measurement applications, leaving detailed explanations of device optics and engineering to other, more topical reviews[21, 22] and the collection of articles from the optics community cited herein.

Specifically, this review will briefly discuss the theoretical basis of high-Q optical sensing, including the multitude of sensor geometries within the category of multi-pass optical sensors. Recent advances in high-Q sensor surface chemistry, capture agent immobilization, assay design, and amplification techniques are covered, as well as interesting demonstrations of these technologies in impact areas such as quantitative detection, affinity profiling, multiplexed sensing, nanoparticle analysis, light manipulation, lasers, thermal sensing, and integrated detection techniques. Finally, we provide our own critical analysis of the field in general, offering thoughts on areas in which improvements are most needed to inform the future outlook and reach the goals of high-Q optical sensing.

Whispering Gallery Mode Sensing

As most of the high-Q optical sensors discussed in this review involve the propagation of whispering gallery modes (WGMs) in microcavities, a brief description of the theory behind this interesting sensing modality is provided first. The whispering gallery phenomenon was initially described by Lord Rayleigh based on observations in St. Paul's Cathedral in London, where he observed that a whisper at one side of the cathedral's dome could be heard on the opposite side of the large room, an effect that is manifested by constructive interference of acoustic waves traveling along the circumference of the dome.[23] WGM optical sensors involve the guidance of photons in a manner that is similar to this acoustic effect. A brief treatment of WGM sensing fundamentals as it applies to an analytical chemistry audience is provided, but we also refer readers to an excellent overview of WGM sensing theory by Vollmer and Arnold.[2]

Microcavity resonators support optical WGMs that circumnavigate the outer edge of a microcavity, confined by total internal reflection at the boundary between the higher-index dielectric cavity and lower-index surrounding medium. The light waves of the WGM constructively interfere as circulating photons return to the point of optical insertion in phase with photons of the same wavelength propagating down an adjacent linear input (fiber optic taper or chip-integrated waveguide). Light is inserted into the microcavity through coupling from a tapered optical fiber (Figure 1A) or adjacent waveguide (Figure 1B), and the light source is typically a tunable laser that is capable of scanning a window of possible resonant wavelengths with high spectral resolution. Only wavelengths of light that meet the constructive interference-based resonance condition are coupled into the microcavity, while all non-resonant wavelengths are transmitted down the adjacent waveguide or optical fiber. The resonance condition for a circular microcavity with radius R supporting a circulating WGM is:

$$m\lambda_r = 2\pi R n_{eff} \quad (1)$$

and demonstrates that an integer (m) number of multiples of the wavelength (λ) must equal the microcavity circumference ($2\pi R$) multiplied by the effective RI (n_{eff}) sampled by the optical mode. In this form, it is clear that changes to either the radius of the microcavity or the effective RI of the optical mode will change the wavelength that fulfills the resonance condition (λ_r). This can be more clearly stated in relative terms of the appropriate variables as:

$$\frac{\Delta\lambda_r}{\lambda_r} = \frac{\Delta R}{R} + \frac{\Delta n_{eff}}{n_{eff}} \quad (2)$$

that highlights that any small relative change in R or n_{eff} must be balanced by an equally small relative shift of the resonance wavelength. From this relationship, it is clear that the relative shift in resonance wavelength, as opposed to the value of the resonance wavelength itself, is the critical parameter for sensing.

The sensitivity to RI changes is based on the interaction of analytes with the evanescent tail of the WGM that extends from the sensor surface into the surrounding medium. As the WGM circumnavigates the microcavity via total internal reflection, an evanescent field extends from the surface of the device according to the electromagnetic wave equation boundary conditions that necessitate a non-zero electric field at the dielectric interface.[3, 24]

The evanescent field strength (I) decays exponentially (with decay constant γ) from its initial value (I_0) with increasing distance (z) from the sensor surface according to:

$$I(z)=I_0e^{-2\gamma z} \tag{3}$$

The strength of the interaction with the analyte near the high-Q sensor, which is proportional to the intensity of the evanescent field extending from the sensor/solution boundary,[25] decreases with distance from the sensor surface and thus has only limited sensitivity to bulk solution contributions.

Since all wavelengths except those that meet the resonance condition in Equation 1 are not coupled into the microcavity and continue to the end of the optical fiber or waveguide, a straightforward optical sensing scheme involves monitoring the transmission spectrum past the resonator, although alternative schemes involving add-drop configurations have been implemented. In the transmission-based detection scheme, resonance wavelengths are observed as dips (negative attenuations) in the transmitted spectrum that are monitored by a photodetector as the laser is tuned through an appropriate spectral window (Figure 1). In order to leverage the potential for high sensitivity detection with high-Q microcavities, extremely small relative shifts in the resonance wavelength (Equation 2) must be measured.

The ability to measure small shifts in the resonance wavelength is enhanced by spectrally narrow resonances. High-Q microcavities are therefore fabricated with precision in order to realize exceedingly narrow linewidths. The Q factor is proportional to the number of times a photon circulates the microcavity[2] and thus determines the effective pathlength over which light-analyte interactions occur.[7] The effective path length (L_{eff}, often on the order of cm) can be described by:

$$L_{eff}=\frac{Q\lambda}{2\pi n_{eff}} \tag{4}$$

and varies directly with the Q factor (typically 10^4–10^8 for high-Q microcavities).[15] The Q factor is mathematically described as the ratio of the resonance wavelength (λ_r) to the spectral linewidth (δλ; full width at half-maximum) of the attenuation peak:

$$Q=\frac{\lambda_r}{\delta\lambda} \tag{5}$$

Therefore, a higher Q factor signifies a narrower transmission attenuation at a given wavelength. Additionally, higher Q factors are associated with a higher photon lifetime (τ) at a given resonance frequency (ω):

$$\tau=\frac{Q}{\omega} \tag{6}$$

The ability to achieve high Q factors in photonic devices is ultimately limited by the capacity to fabricate microcavities that simultaneously maximize the photon lifetime (τ) and minimize both intrinsic and extrinsic power losses due to scattering, radiative losses, bending losses, coupling losses, or poor optical confinement.[26–28] By minimizing surface defects to reduce scattering, carefully perfected dielectric toroidal microcavities have demonstrated Q factors in excess of 10^8 in aqueous environments[29, 30] and photon lifetimes

in the nanosecond regime.[2] It is also worth noting that taking advantage of a high *Q* factor also requires the ability to routinely measure the small $\Delta\lambda_r$ that can be as low as 0.01 pm. Indeed, the ability to control thermal fluctuations, spectroscopic noise, and biological background to levels associated with sub-pm $\Delta\lambda_r$ is a large challenge for all high-Q sensors.

Though the *Q* factor sets the fundamental limit for spectroscopic resolution, spectroscopic noise is often not the dominant source of error for optical sensors applied in useful contexts. Optical engineers and physicists have successfully devoted significant effort toward creating ultra-high-Q microcavities, but interesting real-world applications that require quantitation in truly complex matrices such as human serum, cell culture, or environmental samples remain challenging. Though the multiple interactions with an analyte that are afforded by a multi-pass high-Q optical sensor are vital to achieving impressive surface binding sensitivity, the Q factor sets the limits of sensitivity only when other sources of error are not dominant.

The use of high-Q WGM microcavities for sensing applications is a relatively new field, albeit with somewhat older origins. Though the idea for resonators based on total internal reflection within integrated optics dates from the 1960s,[31] it was not until the 1990s (when micro/nanofabrication techniques came of age) that the use of high-Q ring resonators for telecommunications applications such as optical signal filtering and switching was realized.[32–34] Building on a prediction by Serpengüzel et al. that adsorption of a species to a microcavity would cause a change in the resonance characteristics,[35] the idea of using WGM-supporting microdisks for direct label-free detection of biomolecules was put forth by Boyd and Heebner in 2001.[36] This proposed microcavity device suggested the incorporation of other technologies such as critical coupling[37] and high-level optical integration[38] to achieve a highly sensitive and potentially multiplexable biosensor. Some of these ideas were realized by subsequent reports of the first demonstrations of WGM biosensing based on microsphere,[39] microring,[40] optofluidic,[41] and microtoroid[42] geometries. Though the first demonstrations of biosensing were based on simple adsorption of a model protein to the microcavity and observing the associated shift in resonance wavelength, more sophisticated experiments have followed over the past several years. These exciting recent developments in the field form the basis of this review.

In order to demonstrate the utility of WGM microcavities for applications such as biological, environmental, chemical, and biomedical sensing, many key technical advances have recently been made. These technical advances include developments such as temperature compensation,[43, 44] methods for sensor multiplexing,[45–47] and evanescent field profiling and electric field distribution optimization[3, 24, 48] that are imperative to creating an analytically useful device. Beyond improvements to existing microcavity geometries, innovative device geometries such as adiabatic microring resonators with lossless contacts,[49] concentric nanocavities with sub-/super-radiant modes,[50] and cascaded ring resonators that take advantage of the Vernier effect[51] have recently been proposed. In addition to discussing improvements in device fabrication and materials for various microcavity and photonic crystal geometries, new developments in surface chemistry and assay methodologies that are equally, if not more, critical to the realization of highly specific and multiplexed chemical and biomolecular sensing are covered. Finally, the many interesting recent applications of high-Q optical sensors are covered, highlighting the technical and methodological advances that make these technologies applicable to performing biomolecular assays, monitoring reaction kinetics, sizing and transporting nanoparticles, and manipulating light, among others.

High-Q Optical Sensors: Geometries, Fabrication, and Instrumentation

There are a variety of microcavity geometries that are capable of supporting WGMs, including spheres, toroids, disks, rings, cylinders/capillaries, and slot waveguides. These can be fabricated using a variety of materials, including glass, quartz, silicon, silicon-on-insulator (SOI), silicon nitride, polymers, and various hybrid materials. Among photonic crystal sensors, 1-dimensional, 2-dimensional, and 3-dimensional confinement is possible with a variety of materials that allow high index contrast with periodic modulation. The most common geometries are covered while focusing on recent developments in fabrication techniques, newer designs, and accompanying read-out instrumentation.

Microsphere resonators

Vollmer et al. demonstrated the fabrication of glass (silica) microspheres (~300 μm in diameter) by melting the tip of a stripped single mode fiber into a spheroid-on-a-stem structure with a butane/nitrous oxide torch.[39] WGM resonances were excited by carefully placing the microsphere within optical coupling distance of a HF-etched single-mode optical fiber connected to a tunable distributed feedback laser diode with emission centered at 1340 nm. Using an InGaAs photodiode to detect light intensity transmitted past the resonator through the coupling optical fiber, Lorentzian-shaped resonance peak minima were detected with a parabolic fit and tracked as a function of time. With a measured Q factor of ~2×10^6, additional microsphere experiments were conducted on quartz microspheres of sizes between 88 and 232 μm.[25] Similar experiments involving a microsphere-on-a-stem adjacent to an etched optical fiber have also been used in more recent, real-time experiments aimed at biomolecule detection and protein conformation analysis that will be discussed in subsequent sections.[52–54] One important consideration in these experiments is that the position of the microsphere relative to the optical fiber must be rigorously maintained, as any movement of the microsphere could compromise detection of the resonance.[55] More recent work has centered on fabricating smaller microspheres with larger relative shifts that enable discrete particle binding assays. 100-μm silica microspheres (Figure 2A) are also fabricated from tapered optical fiber tips, but this time by melting with a 10-W CO_2 laser.[56] After suspending this spheroid-on-a-stem structure in a sample cell constructed from o-rings and glass coverslips, and tuning the 763-nm distributed feedback laser wavelength across one or more resonances, transmission spectra were collected with 10–20 ms time resolution (Figure 1A).[56, 57] Temperature and humidity were controlled by enclosing the sample cell. While this experimental configuration is reliant upon careful device fabrication and precise alignment of the optical fiber and the adjacent microsphere, excellent quality factors and single-particle detection experiments, which will be highlighted in subsequent sections, are possible with microspheres.

Other microsphere materials and experimental configurations have also been demonstrated. For example, rather than suspending the microsphere-on-a-stem within a static droplet, a flow-based experiment has been realized by mechanical immobilization of a ~100-μm poly(methyl methacrylate) (PMMA) microsphere within photolithographically-defined Invar channels.[58] In this setup, a prism is used in place of an etched optical fiber to couple light and excite multiple modes in the PMMA microsphere. These experiments are complicated by the need to maintain the position of the microsphere with a microneedle and by the required collection of a complex multi-modal transmission spectrum by a CCD camera. Instead of fashioning microspheres wholly out of PMMA, it has also been proposed that glass microspheres could be coated with a sub-micron layer of PMMA to improve the thermal stability of the sensors.[59] An added advantage of this strategy is that PMMA is a low optical loss material, thus not compromising the Q factor. PMMA has a thermo-optic coefficient that is opposite in sign to that of silica (and silicon), meaning that appropriate coating thicknesses might allow for an elimination (or at least reduction) of temperature-

induced resonance drifts, which often impose fundamental limits of sensitivity in WGM measurements. A high-surface area nanoporous zeolite coating on a silica microsphere has also been proposed for its potential to adsorb analytes such as gas molecules with improved sensitivity.[60] Other examples of polymeric microspheres include the use of ~5-μm polystyrene spheres for WGM sensing based on intrinsic polystyrene fluorescence,[61] emission from fluorophore-doped polystyrene,[62] or on emission from embedded CdSe/ZnS quantum dots.[61, 63] These studies utilize an elaboration of Mie theory[64] to explain the scattering interaction between plane waves and microspheres that allows WGM excitation without evanescent coupling from an optical fiber or prism. Though these methods open the possibility of remote sensing, they require a complex algorithm to analyze the multiple microsphere modes, and their associated Q factors (~2000) are relatively small.[61] It should be noted, however, that "low-Q" microspheres benefit from larger resonant wavelength shifts and decreased spectral mode density, which may actually be advantageous in some circumstances.[62]

Microtoroid resonators

Ultra-high-Q toroidal microcavities were first fabricated by Armani et al. on oxide-coated Si wafers through a combination of photolithography, wet and dry etching, and laser reflowing.[29, 65] Specifically, photolithography is performed on a Si wafer containing 2 μm of thermally grown oxide to define 160-μm photoresist pads that act as a mask during the subsequent buffered HF etch. Photoresist removal leaves behind SiO_2 disks, and an isotropic XeF_2 dry etch undercuts the oxide disks to create Si pillar structures under the disks. The final CO_2 laser reflow step selectively heats the periphery of the SiO_2 disk, causing the formation of a surface tension-smoothed and optically isolated toroidal structure as the disk shrinks. This reflow step effectively removes lithographic flaws and allows tremendously high Q factors (>10^8) to be achieved.[29] Microtoroid sensing experiments require precise alignment of a tapered optical fiber for excitation of WGMs using a tunable laser in the optical telecommunication band (~1500 nm). Only through incredibly careful alignment of the separation distance and tilt angle of the fiber taper with respect to the toroid could low-loss critical coupling be achieved. Though the original microtoroids had a final diameter of 120 μm, subsequent work has demonstrated a range of diameters of 30–150 μm (Figure 2B).[42, 66]

Toroidal microcavities can also be fabricated from other materials. PDMS can be cast around the aforementioned silica microtoroid structures and subsequently filled with thermal- or UV-curing polymer in order to create replicates.[66] Though the PDMS molds can theoretically be used to replicate polymeric toroids many times over, structural imperfections limit the Q factor to 10^5. By combining traditional silica microtoroids with a thin (~100 nm) layer of a polymer applied by spin coating, hybrid silica-polymer microtoroids have also been demonstrated.[67] Both polystyrene and PMMA were tested in the hybrid devices, utilizing a thermal reflow for enhanced polymer smoothness that produced material-limited Q factors of ~10^7. Aside from polymer-silica hybrid devices, metal-coated microtoroids have also been proposed for the purpose of concentrating the WGM in the exterior of the device where the external mode is assisted by a propagating surface plasmon.[68] Simulations have shown that silica microtoroids with a 100-nm Ag coating concentrate ~90% of the optical mode in the surrounding medium (i.e. outside the hybrid device), but Q factors for these lossy, metal-coated devices were limited to ~10^3.68 Though not the only important consideration for microcavity devices, a sufficiently high Q factor is critical for measuring the very small shifts in resonance wavelength required for sensitive analysis. Despite efforts to achieve the maximum theoretical and material-limited Q factors of >10^9, microtoroids fabricated on thermally oxidized Si wafers suffer from diffusion of dopants (such as boron) from the Si layer that change the RI and negatively

impact Q.[28] Regardless of whether toroids can achieve even higher Q factors beyond 10^8, the impressive Q factors of both microspheres and microtoroids come at the cost of (1) fabrication processes that are (as of now) difficult to standardize for reproducible, high-throughput, and scalable sensor devices and (2) a requirement for complicated alignment with an optical fiber for WGM excitation.

Microdisk resonators

The first example of microdisks for sensing by Krioukov et al. involved lithographically defined and vertically coupled 30-μm silicon nitride disks.[69] These early microdisk sensors were complicated by multiple radial modes that required interpretation of a complex transmission spectrum. As described above, silica disks can now be produced as an intermediate step in the fabrication of microtoroids.[29] 60-μm silica microdisks on×of ~10^7 if wedge-shaped edges were fabricated by an HF etch.[70] Recent improvements in fabrication methods have further increased the range of cavity geometries that can be achieved, including silicon nitride (SiN_x) microdisks on a pedestal that have been fabricated with a 40-nm slot to increase modal overlap with the sensing environment.[71] To fabricate these slot disks, thin layers of SiN_x (255 nm), SiO_2 (40 nm), and then SiN_x again (255 nm) were deposited by reactive ion beam sputtering on a Si wafer and annealed. After coating with a Si etch mask, 15-μm disks were created by photolithography and dry etching, and then undercut with a hot KOH etch to define a 3-μm support pedestal below the disk. Finally, the slot was produced by selective etching of the SiO_2 layer. By coupling infrared light from a tunable laser into the disk through a bent, tapered optical fiber, a scattering-limited Q factor of ~10^4 was demonstrated with 21.6% of the mode confined within the slot.[71] Aqueous measurements demonstrated a resonance wavelength peak shift resolution of 78-pm.[72]

Microdisks can also be fabricated from high-index chalcogenide glass materials, such as As_2S_3 and $Ge_{17}Sb_{12}S_{71}$, which can be thermally evaporated onto silicon. Microdisks fabricated from these materials were optically accessed by 800-nm wide bus waveguides in a pulley coupler design in which the waveguide wraps around the planar microdisk.[73] The horizontal pulley-coupled chalcogenide disks relax coupling tolerances, and the entire device was fabricated in a single lithographic step. These unsupported chalcogenide structures can be interfaced with PDMS microfluidics and permit easily fabricated 800-nm gaps between bus waveguide and microdisk, while maintaining an aqueous Q factor of ~2×10^4. Planar devices such as the unsupported microdisk design allow more consistent coupling with the adjacent bus waveguide, removing the requirement for careful alignment with an optical fiber that is required for pillar-supported toroids/disks and microspheres.

Other variations of microdisks that have been recently realized include polymeric and metal-capped microdisks. PMMA microdisks are fabricated by spin-coating 1 μm PMMA on a Si wafer, patterning into ~50 μM disks by standard UV or electron beam lithography, and isotropically etching with XeF_2 to form a pillar-supported microdisk.[74] A PMMA thermal reflow reduces surface roughness and creates a conical disk geometry that supports Q factors of ~10^6. Alternatively, metal-capped microdisks allow for the creation of surface-plasmon-polariton (SPP) WGM cavities (Figure 2C).[27, 75] Using wedge-shaped silica microdisks described above,[70] Ag is deposited on the disk by sputtering, and SPP WGM's are excited by an optical fiber that passes just under the elevated disk to avoid the Ag coating.[27] Simulation results of SPP modes for a variety of metal thicknesses and microdisk sizes demonstrate maximum Q factors of ~4×10^3; Q factors for these devices are limited by the lossy metal layer.[75] A final interesting cavity geometry that combines the lossless pillar contact of a microdisk with the single-mode coupling properties of microrings, termed adiabatic microring resonators, has also recently been proposed.[49]

Microring resonators

By adding an interior boundary instead of a continuous span of material as in sphere/toroid/disk geometries, annular-shaped microrings permit single-mode excitation at the cost of lower Q factors. Unlike pillar-supported microcavities that require complicated etching and laser reflow processes, microrings and bus waveguides can be more easily fabricated in planar arrays by direct extension of commercial semiconductor processing techniques. Microring sensors have been fabricated from a variety of materials including silicon oxide,[40, 76] silicon nitride,[77, 78] silicon-on-insulator (SOI),[43, 79–81] polymers,[82–84] and plasmonic hybrid materials.[85] Vertically-coupled 120-μm silicon oxide microrings fabricated by chemical vapor deposition (CVD) of Hydex were first demonstrated for sensing by Yalcin et al.[40] Vertical coupling of the input and output waveguides to the microring, as opposed to lateral coupling, prevents exposure of the waveguide to surface treatments and offers easy waveguide-ring spacing control (without lithography/etching) to optimize the coupling gap. These rings demonstrated Q factors of ~10^4, and accompanying transmission scanning instrumentation permitted a 20-pm wavelength resolution.[40] Similarly, a vertically-coupled array of five 100-μm silica rings with U-shaped input and output waveguides, demonstrated the inherent scalability potential and broad biosensing applicability of microrings.[76] Additionally, this work utilized an optical spectrum analyzer, broadband light source, and optical switch to permit sequential channeling of light to each of the five rings with a 15 s/ring scan rate. In addition to silica, 140-μm Si_3N_4 microrings were fabricated by a combination of low-pressure CVD, electron beam lithography, and inductively-coupled plasma etching.[77] Interrogation using a tunable laser light source (1260–1370 nm) revealed a Q factor of 1800 and 50 pm wavelength resolution.

Due to their fabrication using straight-forward commercial processes, SOI microring resonators have attracted considerable attention for highly scalable and cost-effective sensing applications. Through a combination of deep-UV lithography[86] and etching, 200 nm × 500 nm Si waveguides and microrings (along with diffractive grating couplers for free space optical scanning) can be fabricated in the top layer of SOI wafers. A perfluoropolymer cladding layers was used to protect the waveguides and restrict solution access to annular openings over each microring (Figure 2D). 6×6-mm chips, each containing an array of 32 microring resonators (30-μm), are individually addressed by a laterally-coupled single-mode waveguide.[87] Critical coupling of light from an external cavity tunable diode laser (centered at 1550 nm) is achieved by insuring a waveguide-ring gap of ~200 nm, and these microrings demonstrate a ~6-nm free spectral range (FSR; the spectral spacing between resonance peaks) and Q factors of 4×10^4.[43] High-speed optical scanning instrumentation constructed by Iqbal et al. provides the ability to sequentially scan a 12-nm spectral window on all 32 rings in the array with unprecedented scan speeds of ~250 ms/ring.[87] By using a 25 GHz Fabry-Perot etalon as a simultaneous wavelength reference to measure *relative* wavelength shifts (without regard to the absolute wavelength), wavelength shifts (~0.2 pm) far below the wavelength resolution of the laser (~20 pm) can be resolved, which greatly improves the device's limit of detection.[43] The surface binding sensitivity (1.5 pg/mm^2) and evanescent field profile (1/*e* decay length= 63 nm; see Equation 3) for these ring resonators have been empirically determined, agreeing well with theoretical results.[3] Other examples of Si waveguides demonstrate innovative waveguide fabrication and sensor miniaturization. Amorphous Si, deposited by a relatively low-cost damascene process involving CVD of amorphous Si into etched SiO_2 trenches, provides an alternative method for creating Si waveguides.[88] These low-loss amorphous Si structures were shown to have Q factors up to 10^5. Other advances in SOI microring fabrication by De Vos et al. include the ability to limit the microring cavity footprint to <10 μm^2 using small racetrack microrings (Q factor ~ 2×10^4) with input and output waveguides accessed by grating couplers.[80] The high index contrast of SOI microrings (as compared to silicon nitride on silica) allows for smaller ring

footprints without excessive bending losses that reduce the Q factor. Beyond demonstrating the high scalability and small footprint afforded by ring geometries, the work by De Vos et al. also further demonstrates the utility of diffractive grating couplers that permit high alignment tolerances. The ability to insert light into the microcavity without the need for careful alignment of a tapered optical fiber is a clear advantage of planar microrings over other geometries.

Microring sensors fabricated from polymeric and plasmonic materials have also been demonstrated. Polymer microrings fabricated from materials such as polystyrene, polycarbonate, PMMA, and SU-8 in both single- and double-coupled variations were achieved using a nanoimprint lithography technique developed by Chao et al.[82, 89, 90] For these polymeric structures, a silicon mold was first created by electron beam lithography and reactive ion etching (RIE).[89] Polymeric microstructures were stamped on a polymer-coated Si substrate, residual polymer was removed by O_2 RIE, and an HF etch was used to form pedestals under the polymer rings and bus waveguides. A thermal reflow technique, analogous to the silica laser annealing method of Armani et al.,[29] was used to improve the Q factor to 2×10^4 in the IR.[82] 800-μm polymeric microrings have also been demonstrated in a vertically-coupled geometry with an embedded polymeric waveguide, yielding a Q factor of 10^4.[84] Beyond polymers, hybrid plasmonic devices have also been proposed.[85] Building off of work on hybrid plasmonic waveguides that impressively confine surface plasmon polaritons,[91] hybrid plasmonic ring resonators combined a Si bus waveguide with a 2-μm Si ring surrounding a metal (Au) disk core. A hybrid mode results from coupling of the silicon photonic and surface plasmonic modes in the metal-Si gap, creating strong RI sensitivity and improved optical confinement within a very small footprint.[85]

Beyond the traditional ring resonator design of a circular waveguide within coupling distance of a linear or bent waveguide, innovative microring designs have been proposed. These designs include racetrack geometries that contain a straight segment within the ring to improve coupling efficiencies,[80, 88, 92] cascaded geometries that allow multiple sensors to be swept with a single wavelength scan,[93] concentric microrings for higher sensing surface area,[94] folded spiral geometries for enhancing the Q factor within a small footprint,[79, 95] and notched ring geometries that improve mode splitting for single-particle detection.[96] Each of these geometries still leverages the relative ease of coupling light into planar device configurations.

Optofluidic, microcapillary, and microtube resonators

Though microrings have demonstrated the ability to be interfaced within microfluidic channels by adhering PDMS[45, 93, 97, 98] or gasket-defined channels[3, 87] on to the device-containing substrate, optofluidic geometries directly incorporate the fluidic function into the sensor itself. Glass optofluidic resonators (known as liquid-core optical ring resonators or LCORR) were first reported by White et al. as a novel technology for combining photonics with well-established capillary fluidic handling.[99, 100] WGMs are excited in a circular cross section of a fused silica capillary by using a perpendicularly aligned tapered optical fiber (Figure 2E). RI changes within the capillary core are probed by the evanescent field that interacts with molecules near the inner wall. To produce the necessary thin-walled capillary, a ~1-mm glass capillary was drawn while heated in a flame to a diameter of ~100 μm, and then wall thickness was reduced to ~3 μm by HF etching.[99] Alternatively, a mechanically controlled method utilizes two translational stages and two CO_2 lasers focused on the capillary in order to direct the temperature and speed at which the capillary is drawn for optimal aspect ratio.[100] Q factors of ~10^5 have been demonstrated for the LCORR device,[24, 99] with device quality limited by surface roughness created during the wall-thinning etch. Typically, experiments are conducted by connecting the capillary to external tubing, and the flow rate is controlled with a peristaltic pump. The sensitivities of the

LCORR to both bulk RI changes[41] and surface binding[24] have been rigorously quantified, and the unique optical mode properties of LCORR and other microtube/capillary devices has also been well-characterized.[48, 101] Additionally, detailed theoretical analyses of thermal and RI sensitivity as it relates to wall thickness for the optical modes characteristic of the microcapillary geometry have been performed.[102] Interestingly, multiple LCORR devices have been arrayed in parallel for such use as on-column capillary electrophoresis detectors.[103]

Variations of the original LCORR device have also been reported. As an alternative to drawing a heated capillary, microtube resonators can be fabricated by a roll-up self-assembly process.[104] In this method, a strained 20-nm Si layer was deposited on a sacrificial Ge layer by molecular beam epitaxy, and a silicon oxide layer was thermally evaporated onto the Si layer. Removal of the sacrificial Ge layer with a hydrogen peroxide etch caused downward bending of the strained Si layer, resulting in a rolled-up Si/SiO_x microtube (~2 μm diameter) geometry that was annealed into an optically active device. Another fabrication method focuses on the ability to create capillaries with sub-μm walls.[101, 105] After first drawing commercial capillaries in a flame to a diameter of ~100 μm, further narrowing and wall thinning was performed with a fiber taper rig while pumping an inert gas to pressurize the capillary. Though Zamora et al. report walls as narrow as 0.6 μm with improved RI sensitivity, Q factors were observed to degrade at sub-μm wall thickness.[101] A very analytically promising variation of the optofluidic resonator involves the fabrication of a micro gas chromatography (GC) detector in a capillary-based optical ring resonator (CBORR) format.[106–108] Similar to the LCORR device, the CBORR device uses a long capillary stretched from a preform under heat to a length of ~10 cm with a wall thickness of 4 μm obtained by a HF etch step. To function as a GC detector, the capillary was coated with a 200-nm polar stationary phase (Carbowax) and joined to a silica guard column that interfaces with a commercial GC injection system.[106] Real-time, on-column gas detection was achieved by placing a tapered optical fiber at a point 6 cm from the CBORR inlet. Gas pulses interact with the stationary phase adjacent to the optical fiber, and multiple tapered fibers at different points on the CBORR allowed for multi-point on-column gas detection to assess separation purity at both the start and end of the column.[108]

Other microcavity resonator geometries

In addition to the multitude of classes and subclasses of high-Q sensors already mentioned, other interesting resonator geometries have been reported in the last few years. These include the hurricane geometry,[109] microbubble resonators,[110] and a variety of slot waveguide designs.[78, 98, 111] The hurricane geometry (Figure 2F) pioneered by Koch et al. uses direct core coupling, which simplifies the device fabrication process by completely eliminating the need for evanescent coupling for WGM excitation.[109] The hurricane device consists of a 20-μm disk structure directly attached to 1-μm-wide input and output bus waveguides, and the device is fabricated in silicon nitride on silica using lithography and RIE. Connection to a broadband power source is performed through polished single mode optical fibers, and lower-cost reflection-mode sensing is also possible.[112] Another interesting microcavity geometry pioneered by Sumetsky et al. involves blowing silica microbubbles from a heated capillary.[110] By rotating a capillary in a CO_2 laser beam, ~370-μm microbubbles with a wall thickness of ~2 μm are formed by radiative heating. The size and wall thickness can be optimized by altering capillary thickness and laser power, achieving a Q factor of ~10^6. The microbubble defines a path for solution flow through the device (as in a microcapillary resonator), preventing disruption of alignment between bubble and optical fiber.

Slot waveguide sensors (Figure 2G) have also garnered substantial interest due to their ability to create a nanoscale area of high WGM localization, yielding an increased field

overlap with the sample volume than conventional rectangular waveguides.[113] By careful fabrication of two high-index waveguides separated by a sub-wavelength (~200 nm) low-index (i.e. air) slot, the dual-core device selectively supports only the lowest order TE and TM modes.[14] A large portion of the TE mode is confined to the slot where it overlaps with the sensing region or sample. Slot devices have been fabricated in a variety of geometries and materials, including Si_3N_4–SiO_2 slot waveguide ring resonators,[77] SOI double-coupled slot racetrack microrings,[111] multiplexed etched silicon nitride slot microrings on a Si substrate,[14, 44, 98] and horizontally slotted silicon nitride microdisks.[71, 72] The multiplexed silicon nitride slot microring device demonstrated by Carlborg et al. provides the best example of integrated slot waveguides to date.[98] By using standard silicon fabrication on a thermally oxidized Si substrate with 300 nm silicon nitride deposited by CVD, silicon nitride optical components were patterned by electron beam lithography and dry etching. A silica cladding layer was then added by CVD, and optical access points opened by HF etching. The device also used a grating coupler for optical insertion into the device, and a multimode interference splitter provided access to an array of 8 rings. Double-slot microring devices have also been studied, and optimization of fabrication considerations suggests that double-slot rings actually have higher fabrication tolerances than single-slot rings.[114]

Photonic crystals and surface plasmon cavities

Though not generally considered high-Q sensors in the strictest sense of the definition, photonic crystal structures can similarly support multi-pass label-free sensing and optical confinement that is analogous to their higher-Q WGM counterparts. Photonic crystal sensors generally have Q factors between 10^1–10^3,[46, 115, 116] although notable examples of high-Q photonic crystal geometries have been demonstrated recently with Q factors of 10^4–10^7.[117–119] Due to these recent improvements in Q factor and also the highly complementary advances in surface chemistry and assay methodology that are relevant to microcavity sensors, photonic crystal sensors and photonic-plasmonic hybrid devices are briefly introduced here.

Photonic crystals are composed of two materials with different refractive indices that are periodically modulated in one, two, or three dimensions.[4, 120] A variety of geometries, including 1-D,[6, 46, 115, 121] 2-D,[122–125] and 3-D[119, 126] structures have been demonstrated in material systems such as TiO_2/SiO_2,[127, 128] SOI,[118, 129] GaAs,[130] and hybrid plasmonic/photonic components.[131] Though many manifestations of photonic crystal architectures have been demonstrated, only the 1-D geometries are discussed as they have found the most widespread use as optical sensors.

Fabrication and signal transduction for 1-D SOI photonic crystals are very similar to some of the microcavity devices already discussed, but do not involve WGM propagation. By a combination of lithography and etching techniques, 1-D Si photonic crystal structures containing a central defect cavity and 16 ~200-nm resonant holes are patterned adjacent to an input waveguide (Figure 2H).[46] The central cavity creates a defect in the photonic bandgap that determines a specific optical resonance, and a large portion of the resonant optical mode resides in the photonic crystal holes ($1/e$ distance = 80 nm from hole wall).[46] Changes in the RI at the surface adjacent to the holes lead to a shift in the resonant wavelength, similar to the aforementioned high-Q geometries. Other important photonic crystal fabrication techniques utilize a polymer substrate fabricated by replica molding under a 1-D periodic grating structure composed of TiO_2/SiO_2 (Figure 2I).[127, 128] Broadband illumination excites an optical mode that is guided in the high-index TiO_2 layer and extends into the sensing media above the device surface. The resonance condition is observed as a dip in the transmission spectrum for both TE- and TM-polarized light.[128] The periodic structure can also be thought of as a reflective optical filter where only specific combinations of incident wavelength and incident angle of the exciting light source are

reflected.[132] Though fabrication techniques, dimensionality, and geometries vary widely, the myriad of photonic crystal and microcavity devices are connected by their ability to support highly efficient light-matter interactions at precise resonant wavelengths.

Surface Chemistry, Device Functionalization, and Capture Agents

After careful fabrication of an optical sensor that supports high-quality modes, surface chemical functionalization must be utilized to confer specificity for a particular analyte. Though many devices with high Q factors have been demonstrated, only a handful of devices have been applied to real-world detection challenges. Regardless of the narrowness of the resonance, high-Q devices will only meet their full sensing potential with highly optimized surface chemistry and functionalization techniques that support subsequent quantitative analyses.

Selection of capture agents

It is important to highlight at the outset that, for many bioanalytical applications, the ultimate sensitivity and specificity of the device is fundamentally limited by the properties of the biomolecular capture agents, irrespective of the device sensitivity. For this reason, it is desirable to obtain capture agents with high affinity, selectivity, and stability. The most commonly used capture agents for biomolecular analysis include antibodies, antibody fragments, complementary DNA (cDNA), and aptamers. While antibody production relies on immune challenge and hybridoma formation, nucleic acid capture agents can be obtained from solid-phase DNA synthesis or multiple rounds of selective enrichment (SELEX) to identify or evolve the most effective capture agent. Beyond the capture agent itself, careful attention must be paid to the manner by which surface attachment is achieved, as consideration of such factors as molecular orientation, specific attachment site, and capture agent stability over time may greatly influence the sensor performance. If a sensor array is to be multiplexed, a quality that is often very desirable when multiparameter analysis provides increased information from a single sample, the potential for capture agent cross reactivity is an additional concern. Spatial control over functionalization must also be maintained. The following discussion of chemical methodologies for imparting unique surface chemistry describes important recent advances in device functionalization for a variety of targets.

Physisorption and streptavidin-based attachment

The most straightforward method for capture agent functionalization involves simple physisorption of a biomolecule that recognizes a particular analyte onto the sensor surface. This non-covalent method for capture agent immobilization provides a simple route to proof-of-concept biosensing results, but physisorption has limitations for complex assays that require reproducible surface blocking and efficient surface regeneration. Several of the pioneering WGM biosensing demonstrations with microspheres and microtoroids were based on simple adsorption of biotin,[30, 42] Protein G,[30, 42] or biotinylated bovine serum albumin.[39] In these formats, the initial biomolecular physisorption provided a handle (biotin, Protein G) to recognize binding partners such as streptavidin or IgG molecules. Tetravalent streptavidin can also be adsorbed or bound to biotinylated surfaces for subsequent immobilization of biotinylated capture probes[133] or biotinylated Protein A.[115] Though important for demonstrating the sensing capabilities of high-Q sensors, more advanced assays have implemented robust, specific, and reproducible surface chemical treatments.

Covalent capture agent functionalization chemistry

Covalent attachment of capture agents is widely thought to provide the best stability and durability in the face of changes in ionic strength, pH, temperature, and flow rate that accompany many assays. Due to the abundance of silicon and silica materials in the field of

high-Q sensors, the vast majority of covalent functionalization techniques centers on the use of silane chemistry. Initial work with silane chemistry involved the deposition of (3-Aminopropyl)triethoxysilane (APTES) or (3-Aminopropyl)trimethoxysilane (APTMS) to provide amine functionality.[40, 43, 46, 72, 80, 87, 100, 134, 135] 3-(Glycidyloxypropyl)trimethoxysilane (GOPTS) has also been used to a lesser extent to form an amine or sulfhydryl-reactive epoxide surface.[76, 111, 127, 128] Silane deposition can be effectively carried out in solvents such as ethanol, dimethylformamide, isopropanol, toluene, or acetone using flow-based, vapor phase, or spotting methods. Amine-functionalized sensors can then be functionalized with amine-reactive *N*-hydroxysuccinimide (NHS)-biotin[3, 43, 72, 80, 134, 136] or succinimidyl-6-hydrazino-nicotinamide (S-HyNic).[87, 135] Indeed, by incorporating amine functionality, a variety of bioconjugation strategies for capture agent attachment are possible. As an added benefit, high-Q sensors permit real-time monitoring of silane deposition to verify reproducible surface coverage. Since silanization is often a disordered process, it is likely that multiple layers of silane are deposited onto the sensor surface[40] unless reactions are performed with extreme care, although multilayer silane deposition does not necessarily preclude successful device operation. Nonetheless, techniques such as vapor-phase silane deposition[47, 127, 128] and sonic agitation[137] have been used in attempts to achieve a more ordered surface with reproducible binding capacity, and special care has been taken to ensure maintenance of the Q factor (Equation 5) during silanization and subsequent steps.[136]

Once silanization provides a foundation for bioconjugation reactivity, surfaces can be covalently modified with capture agents such as antibodies, cDNA, or aptamers with crosslinking chemistry based on glutaraldehyde,[98, 138, 139] hydrazone bond-forming HyNic/4-formyl benzamide (4FB) cross-linking,[43, 87, 135, 140] or 1-ethyl-3-(3-dimethylaminopropyl)carbodiimide (EDC)/NHS.[6, 100, 115] In each case, amines on the device surface are coupled with amine or carboxyl groups on the capture agent. Antibodies contain amine-terminated amino acids (such as lysine residues and the N-terminal amino acid) as well as carboxy groups (such as aspartate and glutamate residues, as well as the C-terminal amino acid), and cDNA probes can be directly synthesized with a 5'-amine termination. Glutaraldehyde acts as a homobifunctional linker to join capture agent amine groups to aminated silane or silicon nitride surfaces, although reactions between glutaraldehyde oligomers can also achieve capture agent attachment.[141] However, the resulting Schiff base formation by the reaction of aldehydes and amines is reversible and thus should be further reduced with a reagent such as sodium cyanoborohydride to the secondary amine for increased attachment stability. Similar homobifunctional amine cross-linking has also been demonstrated with dimethyl adipimidate (DMA),[142] dimethyl pimelimidate (DMP),[143] and disuccinimidyl carbonate (DSC).[97] In the case of HyNic/4FB cross linking, amine groups on the surface and capture agent are functionalized with hydrazine and aldehyde moieties, respectively, which then react to form a stable hydrazone bond to link the capture agent to the surface. Notably, this linkage, which involves an alpha-effect nitrogen in the hydrazine (also in aminoxy groups), directly forms an irreversible bond between the capture agent and sensor surface that does require further reduction. The hydrazone bond-forming reaction proceeds more rapidly at lower pHs, although aniline has been shown to catalyze this hydrazone bond formation effectively even at neutral pH.[140] Additionally, a commercially available HyNic-silane reagent can be used to deposit a hydrazine moiety on the sensor surface in one silanization step.[144, 145] In the case of EDC/NHS chemistry, antibody carboxyl groups are converted to amine reactive NHS esters. Sulfo-NHS can be used to improve solubility in aqueous solutions,[100] and NHS ester formation stabilizes the *O*-acylisourea intermediate that is susceptible to hydrolysis. Succinic anhydride can also be used to convert amine-terminated silanes to carboxyl groups for subsequent EDC/NHS coupling to protein amines.[115] These conjugation reactions,

among other possibilities, provide a range of functionalization approaches that are highly amenable to high-Q sensors.

Other methods for capture agent functionalization of sensor surfaces

Recently, several useful and innovative conjugation strategies have been applied to high-Q sensors, and these involve the use of dendrimers,[6] dextran hydrogels,[133] Si-binding proteins,[146] plasma-based polymer functionalization,[147] and Ni-NTA chemistry.[148] Dendrimers are known to improve DNA immobilization efficiency while maintaining high stability,[149] and Goddard et al. used carboxy-terminated generation 4.5 dendrimers linked to APTMS via EDC/NHS chemistry on a 1-D photonic crystal surface as tethers for DNA probes.[6] They show that negatively charged dendrimers can electrostatically repel non-specific DNA binding, prevent deleterious surface effects that restrict analyte binding, and lessen steric hindrance. Another method to improve capture agent immobilization efficiency makes use of a biotinylated dextran hydrogel, and Vollmer et al. utilized this approach to immobilize streptavidin-conjugated DNA capture probes at a density of 4.6×10^{13} probes/cm^2.[133] In order to attach proteins directly to silicon photonic sensors, another innovative approach takes advantage of a silica-binding protein called Si-tag that facilitates direct attachment of recombinantly expressed protein capture agents to silica surfaces, thereby eliminating the requirement for chemical modification (such as silanization).[150] Furthermore, the Si-tag (a fusion protein of silica-binding bacterial ribosomal protein L2 with a capture agent or ProteinA) should provide control over capture agent orientation and thus has the potential to prevent the loss of binding activity this is unavoidable when using non-oriented immobilization methods.[146] Outside of silicon-based photonic structures, polymer-based high-Q devices can be functionalized by oxygen plasma treatment. O_2 plasma treatment of PMMA, SU-8, polycarbonate, and polystyrene was demonstrated as an effective method to introduce carbonyl, carboxyl, or hydroxyl functionality to polymer devices.[147] Finally, device functionalization using Ni^{2+}-nitrolotriacetic acid (Ni-NTA) surface chemistry for immobilization of histidine-tagged proteins provides a useful handle for studying recombinant proteins. Heeres et al. synthesized a biotin-tris-NTA molecule to functionalize a streptavidin-coated photonic crystal device, and Ni^{2+}-charged surfaces were used to study protein-protein interactions.[148] Each of these alternative functionalization strategies successfully demonstrates the merits of optimizing surface chemistry for defined sensing applications in aqueous environments.

High-Q sensor functionalization for gas sensing applications

Beyond aqueous-phase sensing, innovative surface chemistry has also been developed for gas sensing applications. The discussion of optofluidic sensors included a potentially very powerful application of this technology for gas chromatography based on introducing a stationary phase polymer coating to the surface of a microcapillary resonator.[106–108] Related optofluidic sensors have been coated with poly(ethylene glycol) (PEG)-1000 and used for vapor detection of the explosive DNT.[151] A microcapillary was soaked in a methanolic solution of PEG-1000 for 1 h, followed by solvent evaporation under vacuum. Various PEG-1000 concentrations were tested to achieve an optimal and uniform PEG-1000 thickness of 60 nm.[151] In addition to the gas chromatography surface chemistry, other methods also permit detection of important explosives in vapor, such as a silicon nitride microring that was functionalized with a triphenylene-ketal receptor/cladding layer for reversible and selective TNT vapor detection.[152] In this instance, the 150-nm receptor layer was applied by an electrospray method utilizing tetrahydrofuran as solvent and a metal cannula with an applied voltage of 5 kV.[153]

Beyond the detection of vapor-phase explosives, high-Q gas sensors have also been functionalized with coating materials such as ZnO nanoparticles,[154] a Pt-doped tungsten

oxide catalyst,[155] and a zeolite.[60] These examples utilize inorganic adlayers on the photonic device in order to increase the surface area probed by the sensor, which permits elucidation of measurable wavelength shifts even at low analyte concentrations. A uniform and porous 200-nm layer of ZnO nanoparticles, with deposition controlled by photoresist-localized drop casting, provided a high-surface area coating for ethanol vapor sensing on a SOI microring platform.[154] ZnO was also chosen for ethanol sensing due to its high affinity for volatile compounds, low cost, and transparency in the near infrared, which is critical for the maintenance of high microring Q factors ($> 10^4$). Catalytic materials have also been employed as coatings for gas sensing. A Pt-doped WO_3 catalyst was deposited by dip coating fully silica-coated SOI microring into a sol-gel solution, yielding a few-μm-thick catalytic layer.[155] The Pt-doped WO_3 material provided a platform for catalytic H_2 combustion that leads to an 80-pm/K resonance wavelength shift by the thermo-optic effect. Additionally, the crystalline aluminosilicate zeolite has, due to its (sub)nanometer-scale pore size, also been proposed as a sensitivity-enhancing coating for microsphere resonators. A zeolite layer could enhance the sensitivity by increasing sensor surface area and effectively trapping adsorbed vapor-phase chemical analytes.[60] Despite these few important advances, the use of high-Q sensors in vapor detection challenges remains largely underdeveloped and thus looms as a potentially fruitful application area. Aqueous-phase sensors have dominated the high-Q sensor landscape due to the heavy focus on biological and biomedical applications, and more advances in surface chemistry for vapor sensing will likely be required to enable important homeland security and environmental monitoring applications.

Directed immobilization of capture agents by microfluidic and high-precision spotting methods

All of the methods described thus far have focused on bulk, uniform functionalization of a high-Q sensor substrate without spatial control. Bulk functionalization is suitable for many applications, but directed capture agent immobilization methods are needed in order to fully leverage the promising multiplexing capabilities allowed by highly scalable high-Q sensor geometries. Planar and near-planar devices with small footprints are most amenable to microfluidic and microspotting approaches for spatially directed surface derivitization.

Microfluidics based on PDMS and fluidic cartridge/gasket designs have been demonstrated, especially for multiplexed SOI microring and 1-D photonic crystal devices.[45, 46, 87, 93, 98, 156] For multi-element micron-scale sensor arrays, microfluidics are well-suited to delivering specific capture agents to individual sensors or groups of sensors. After a bulk silanization or other chemical functionalization step, sensors can be selectively functionalized with various capture agents. For example, Washburn et al. used 6-channel PDMS fluidics to functionalize 6 groups each containing 4 microrings with unique capture antibodies (Figure 3A).[45] Similarly, a 5-channel PDMS device was used by Mandal et al. for localized immobilization of capture antibodies and a control protein on an array of 1-D photonic crystals.[46] PDMS fluidics, though widely used, suffer from the need to align each custom device and then achieve leak-free adhesion to the sensor device surface. Conversely, packaged fluidic cartridges can allow routine, reproducible, and reusable device/fluidic alignment. A multi-channel fluidic design based on a 0.007”-thick Mylar gasket sandwiched between a sensor chip and a fluidic cartridge with input and output ports has allowed for deposition of up to 4 capture agents, including such classes as antibodies, aptamers, or cDNA, on independently addressable groups of rings.[156, 157]

Other spatially directed capture agent immobilization techniques take advantage of hand-spotting,[47, 76, 135, 137] piezoelectric (inkjet),[158] or lithographic[159] printing techniques. Hand-spotting techniques can have mm-scale resolution with a simple plastic micropipette tip[137] or 100-μm resolution with the use of a microcapillary mounted on a translational stage and guided by a stereoscope.[159] Alternatively, non-contact inkjet printing dispenses pL-sized

droplets from a glass capillary with fine positional control for individual functionalization of multi-sensor arrays on silicon photonic devices (Figure 3B).[47, 95, 97, 134, 158, 160] A potential complication of spotting, particularly as it applies to protein-based capture agent deposition, is the denaturation and instability of the capture agent when the spots dry. Thus, many successful applications of spotting-based functionalization have used nucleic acid probes,[135, 137] stable model proteins (i.e. bovine serum albumin),[47, 158] or taken special care to control humidity to prevent proteins from drying out.[76] To take advantage of the high stability of DNA probes in the creation of antibody arrays, Washburn et al. employed a DNA-encoding scheme to localize antibodies to specific locations on the basis of nucleic acid hybridization and self-assembly.[161] After cantilever-based lithographic spotting of short 4FB-modified single-stranded DNA (ssDNA) sequences on a bulk HyNic-silane surface containing 32 microrings, the ssDNA array can be used as a stable platform to self-assemble antibodies encoded with orthogonal ssDNA complements (Figure 3C).[159] In this way, antibodies were continuously exposed to an aqueous microfluidic environment, rather than dehydrated during spotting, and directed to specific microrings based on the complementarity of their cognate ssDNA.

Non-fouling surface modifications

A majority of contemporary, real-world sensing applications necessitate analysis within complex matrices such as serum, cell culture, or environmental samples. This complication is particularly profound for many RI-based detection strategies described herein as the universal detection characteristics of label-free sensors make the analytical challenge akin to finding a "needle in a haystack," but where there is no contrast in terms of response between the needle and hay. Sensor specificity is largely achieved by selection of target-specific capture agents, but there is also interest in deploying anti-surface fouling chemical coatings that help discriminate specific signals from a complex background. Poly(ethylene glycol) (PEG)[162] and zwitterionic polymer brushes[163] are two surface coatings known to inhibit non-specific adsorption, especially for biological samples. De Vos et al. demonstrated the use of ~2-nm-thick carboxy- and amine-terminated PEG layers on silanized SOI microrings to resist non-specific binding of BSA.[97, 164] Additionally, the zwitterionic polymer brush poly(sulfobetaine methacrylate) (pSBMA) was grown directly on SOI microrings by Limpoco and Bailey using atom transfer radical polymerization (ATRP). The non-fouling pSBMA surfaces were generated with controllable thickness and reduced non-specific binding in undiluted fetal bovine serum to 260 pg/mm^2 (compared to 1400 pg/mm^2 for PEGylated surfaces).[165] Though PEG and pSBMA greatly reduce non-specific binding, the high sensitivity of microcavity sensors to surface binding (LOD~1 pg/mm^2)[3, 24] means that for even the highest performance non-fouling surfaces, readily detectable amounts of non-specific protein binding will always be observed during analysis of highly complex samples (e.g. serum). For this reason, effective surface blocking processes and proper controls are essential components of assay development.

Real-time monitoring of surface chemistry

It should be noted that label-free sensors, which often permit real-time sensing, can provide vital information for studying surface reactions such as silanization,[43, 81, 135] capture agent loading,[45, 138, 140, 156, 159, 166] and polymer growth processes.[3, 46, 165] Apart from the obvious utility for label-free sensing, the ability to observe surface chemistry in real time has been utilized for optimizing covalent antibody ligation catalysis,[140] ensuring reproducible capture agent density,[159] and comparing polymerization kinetics for various conditions.[165] Beyond screening reaction conditions and monitoring surface chemistry, real-time binding analysis also provides an effective means for sensor characterization by mapping the evanescent field decay.[3, 46] By alternating positively and negatively charged polymer electrolyte layers of known and consistent thickness, the decrease in signal intensity with

increasing distance from the surface (Equation 3) is due solely to the evanescent field decay properties of the optical sensor (FIGURE 4A). Using this strategy, the 1/*e* distances of the evanescent field, which is a vital metric for optimization of capture agent presentation, were determined for both SOI microring resonators (63 nm)[3] and 1-D photonic crystals (80 nm).[46] Notably, the high RI contrast between the silicon-based optical cavities and the surrounding environment gives an exceptionally rapid decay of the evanescent field that signifies enhanced surface (as opposed to bulk solution) sensitivity. Based on the determined evanescent field decay constant, microrings have also been used to probe more complex protein multilayer growth patterns (Figure 4B).[3]

Surface regeneration

A variety of methods for chemical and biological functionalization of sensor devices have been described, but once functionalized, for some applications it is desirable to reuse the same functionalized surfaces in consecutive assays. Furthermore, once a device is fabricated, it may be desirable to use the device to study a different target in a similar assay, or for an altogether different application. Thus, maximizing the utility of a high-Q sensor requires the ability to both 1) restore the capture agents for inter-assay regeneration, with conditions mild enough to not destroy the capture agent and also 2) totally regenerate the sensor by removing all chemical and biological functionalization.

For inter-assay regeneration that restores the capture agents without destroying them, various techniques have been developed for both protein and DNA capture agents. For regeneration of protein capture agents such as antibodies, a short rinse (1–2 min) using a pH 2 glycine buffer can be used to disrupt some protein-protein interactions.[45, 87, 124, 145] To regenerate DNA capture probe surfaces by breaking DNA-DNA interactions, the chaotropic reagent 8M urea can be introduced to disrupt hydrogen bonding between complementary bases of the target-capture probe duplex.[144] For regenerating RNA or miRNA sensors that utilize DNA capture probes, an enzyme called RNase H was used to selectively cleave only DNA-RNA heteroduplexes, with full regeneration in ~30 min.[135] Aptamer capture agents specific for protein targets can be regenerated with proteinase K that digests the bound protein.[156] Phage capture agents can be regenerated with either an ionic solution (KSCN/$MgCl_2$/urea/guanidine-HCl) or a chelating solution (EDTA).[138] Studies have also been carried out using kinetic titrations for antibody-antigen binding, in which a series of small, non-saturating concentrations are flowed without inter-assay regeneration.[76, 139, 159]

For total device regeneration, harsher conditions are used to remove all chemical and/or biochemical species from the sensor surface. These include the use of hot piranha (3:1 H_2SO_4:30% H_2O_2) solutions,[87, 140, 145] O_2 plasma treatment (120 W, 200 mTorr)[65] to remove all organic molecules, or dilute (1–2%) HF chemical etching,[138, 142, 143] which strips away a thin layer of the oxide surface to which chemicals and/or biomolecules were attached. In our lab, SOI microring resonator chips can be regenerated 10+ times before sensor performance degrades significantly. HF etching of optofluidic microcapillaries allowed 4–5 full regenerations before the capillary wall was compromised,[138] and oxygen plasma-treated microtoroids maintain high Q factors through at least a few regeneration cycles.[65] Though many future application areas for high-Q devices will likely require single-use/disposable sensors that leverage the potential cost-effective fabrication of many device architectures, the ability to regenerate sensor devices remains valuable in both assay development and surface chemistry optimization.

Recent Developments in Assay Design

Once effective surface chemistry has been developed for detection of a particular analyte, assays must be designed and optimized for requisite sensitivity, specificity, and quantitative

utility. Though it is critically important to have high-quality sensors and robust optical scanning instrumentation, useful applications of optical sensors require that tremendous attention is given to surface chemistry and assay design considerations; these considerations have only recently begun to be addressed in the high-Q sensing community. Non-trivial systems and assay integration remain significant obstacles to widespread applications of many of the device architectures described in this review. In order to reach its full potential, high-Q optical sensor technology must be further developed by focusing on assay design considerations and related issues such as matrix effects, temperature and sample background controls, strategies for multiplexed and high-throughput analysis, fluidics integration, and signal amplification for difficult targets. The important recent developments in assay design will be discussed here, and the interesting applications enabled by these assays will be discussed in the next section.

Measurement techniques for high-Q sensing: intensity vs. resonant wavelength shift

The basis for signal transduction has been described in detail in the section about WGM sensing and different device configurations will be discussed in the Recent Applications section. In a typical assay, the interaction of an analyte with a functionalized sensor surface results in a binding-induced change in the RI sampled by the optical mode and a corresponding shift in the resonance wavelength (Equation 1). Despite their high Q factors, resonance spectra of microcavities still have finite line widths, and an early example of biosensing with SOI microrings used the real-time change in transmission intensity at a defined wavelength to monitor binding.[40] This early example of measuring binding responses required the ability to track the intensity at only a single wavelength; however, the vast majority of high-Q sensor work utilizes more complete spectral information.[39, 43, 87, 103] A Lorentzian fit to the transmission spectrum and subsequent mathematical determination of the peak resonance wavelength allows for a more accurate resonance wavelength determination that is not as susceptible to laser intensity fluctuations. Even stable tunable lasers have wavelength uncertainties that are often >20 pm due to variations in laser sweep velocity, but multiple resonances of a fine FSR etalon can be monitored to improve wavelength determination accuracy.[43] In most applications, the relative wavelength shift (as opposed to the absolute resonance wavelength itself) is the metric used for quantitative analysis (Equation 2), and high-Q optical sensor data plots commonly display the relative shift vs. time.

Temperature control

The ultra-sensitivity of high-Q sensors to thermally-induced changes in RI (commonly 10^{-5}–10^{-4} RIU/K) means that any successful assay must account for temperature fluctuations. Differences in thermo-optic coefficients as well as thermal expansion of the device itself are known to lead to a strong dependence of resonance wavelength on temperature, which often limits the sensitivity of high-Q sensors. Indeed, ring resonators have been used as miniature temperature sensors, as described in the subsequent applications section. Reliable temperature control for sophisticated assays must involve more attention than simply allowing samples to equilibrate at room temperature. Even under well-controlled ambient conditions, temperature variations lead to signal aberrations upon sample introduction.[39] Some have addressed the thermal control issue through the use of active temperature control in the form of a Peltier heat pump device and thermistor.[77, 98] Though active temperature control may be built directly into the instrument, as in surface plasmon resonance (SPR) instruments where temperature is controlled to within ±0.01–0.1 K, these systems add complexity, cost, and size to the instrument,[160] and are also insufficient to fully compensate for small, but very detectable temperature fluctuations. Athermal planar waveguide-based SiN and SOI devices was designed such that core and cladding have thermo-optic coefficients with opposing signs, and the structures are designed to balance the

fraction of light propagating in each.[167, 168] However, a more straightforward temperature control method uses on-chip temperature references in thermal contact with functionalized sensors. Gylfason et al. demonstrated the use of on-chip temperature compensation through the use of a separate fluidic channel dedicated to blank buffer samples that act as temperature references.[14, 44] This temperature compensation method, while reducing the temperature sensitivity of their slot waveguide ring sensors from 16 pm/K to 0.3 pm/K, is limited by the ability to maintain equal temperature and bulk RI control between sample and reference solution. This separate channel technique is similar to the reference arm layout for temperature control that has been used for Mach-Zehnder interferometry.[134]

Ideally, however, temperature controls should simultaneously be exposed to the exact solution conditions as the analyte sensor elements. By providing in situ thermal controls that are adjacent to active sensor elements but coated in cladding and unfunctionalized, thermal control elements experience the same ambient or fluidic conditions and are directly adjacent to functionalized sensors, with only a rapidly equilibrating thermal gradient lag as the thin cladding layer transmits temperature from the overhead solution. The most effective on-chip thermal referencing has involved coating one or more Si ring resonator sensors (within the same fluidic channel as sensor rings) with SU-8,[160] SiO_2,[98, 160] or a perfluoropolymer[43, 87] cladding layer. The cladding layer ensures that reference rings respond only to temperature variations, and not to other matrix effect. Implicit in the use of chip-integrated, in situ temperature controls is the need to fabricate multiple identical resonant structures. It is thus no surprise that the best temperature controls have been integrated into planar ring resonator devices that allow for the most straightforward, on-chip sensor multiplexing.

Advances in multiplexed high-Q sensors

The ability to incorporate multiple sensors onto a single device not only allows for in situ thermal controls, but multiplexed sensors that simultaneously assay many target analytes are highly desirable for a variety of applications. Though it is possible to use two microspheres together in a single sensor[133, 169] or to fabricate arrays of microtoroids,[66] non-planar high-Q devices are intrinsically more difficult to simultaneously interrogate in a scalable manner due to complications associated with demanding optical fiber alignment tolerances and the more complex multimodal resonance spectra. Microring resonators have to date been by far the most amenable to sensor multiplexing, with published examples of planar arrays containing 5,[76, 170] 8,[98] 12,[97] and 32 rings[43, 87, 145] that can be monitored simultaneously using separate access waveguides for each ring. Another clever design for using arrays of planar microrings for multiplexed sensing, called wavelength division multiplexing (WDM), utilized multiple microrings of different size but attached to a single waveguide.[47] However, as with using different sized microspheres and a single transmission spectrum with multiple sets of resonance dips, the multiplexing capabilities of WDM devices are potentially limited by the FSR overlap of multiple sensors. For this reason, as well as their relative ease of design and fabrication, configurations with one sensor per waveguide are most common. These small-footprint planar ring resonator devices utilize scalable semiconductor fabrication techniques on SOI substrates, and these devices have the added benefit of relatively easy fluidics integration.

Fluidic strategies for integrated assays

The integration of optical components, high-Q sensors, and microfluidics into a low-cost and automated device represents an important goal for enabling diverse applications such as medical diagnostics, environmental monitoring, and homeland security.[18, 19] Robust fluidics have the potential to reduce sample consumption,[18, 137] automate assays,[3, 159] and increase directed mass transport to address the prohibitive timescales required to detect sub-pM analyte concentrations under passive diffusion conditions.[171, 172] Indeed, recent studies by

Choi et al. carried out with photonic crystal substrates to compare the same assay in microplate, microspot, and microfluidic formats demonstrated the superiority of microfluidics for faster assays with lower detection limits.[173] Optofluidic resonators such as LCORR effectively incorporate a microcapillary into a resonant cavity, demonstrating the most straightforward photonic/fluidic integration.[99, 100] Additionally, rather than unidirectional mass transport from a microfluidic channel down to a resonator sensor, optofluidic resonators take advantage of radial diffusion of the analyte in solution to the capillary wall. Other important fluidic advances involve the use of PDMS[14, 45, 46, 93, 97, 98, 109] or gasket-defined fluidic channels[3, 43, 87, 156] to deliver solutions directly to a specific sensor or a group of sensors for differential sensor functionalization or more complex assay techniques (Figure 3A). In all fluidic strategies, it is important to ensure an effective seal between the fluidic structure and high-Q sensor substrate below. Fluidic channels not only allow spatial control over surface chemistry and faster reaction kinetics, but also offer the potential to greatly improve assay reproducibility[3, 159] and to recirculate an analyte solution to improve capture efficiency in sample-limited applications.[135, 137] Digital fluidic techniques, which use an array of electrodes to manipulate discrete droplets,[174] also have the potential to interface with optical sensors.[175] It should be noted that not all geometries are equally compatible with fluidic integration; it is known that fiber-coupled geometries such as spheres and toroids suffer from hydrodynamic fluctuations that cause unstable fiber taper-to-device coupling.[176] However, planar devices, where the interrogation waveguides are rigidly part of the physical device architecture, are more amenable to fluidic integration. Virtually all applications of high-Q sensors for relevant assays have incorporated a microfluidic component for controlling surface chemistry and/or delivering samples.

Strategies for making relevant measurements in complex matrices

Useful applications of high-Q sensors, such as bioanalysis, require the ability to conduct assays in complex matrices within a relevant analyte concentration regime. These important assays not only often require impressive sensitivity, but the complex sample matrix necessitates the use of carefully designed controls and strategies for improving specificity. High-Q sensors have only recently begun to be combined with carefully constructed quantitative assay strategies for useful targets. The difficulties in transitioning from proof-of-principle sensing in buffer to the realization of detection from within real-world samples, such as human serum or cell culture media, cannot be overstated. Real-world samples often require the ability to differentiate specific responses from a very large background response from non-specific binding. The use of well-blocked sensors reduces non-specific adsorption of biomolecules such as proteins, and sensors are routinely blocked following capture agent functionalization with reagents such as BSA,[45, 46, 76, 87, 138, 140, 145] a mixture of blocking proteins such as BSA and casein,[3, 137, 157] PEG,[139] 10% FBS,[139] protein A,[166] and/or Tween-20.[46] By coating the entire device surface in a controlled blocking step, non-specific adsorption during the assay is avoided. Buffer additives such as Tween and BSA are also often used to continuously re-block the surface during the assay itself, as non-covalent blocking agents are often displaced from the surface over time. After blocking, quantitative assays can be performed (1) on the basis of the pseudo-equilibrium net shift of the binding response after a defined time or (2) the initial slope of the response during the first few minutes of analyte binding. Traditional analytical chemistry techniques such as calibration plots or standard addition analyses are then used to quantitate unknown sample concentrations. If an array of high-Q sensors is available, one or more elements can also be used as a reference for non-specific binding.[45, 145] These control sensors that are not functionalized to be specific for any targets but are exposed to the same sample can simultaneously serve as controls for temperature fluctuations, bulk RI changes, and non-specific binding that is common in complex samples such as serum.

Sensing in serum or serum-containing cell media, for example, often decreases the limit of detection of the assay by roughly an order of magnitude due to difficulties in fully eliminating or correcting for non-specific adsorption. For example, in a direct, label-free assay involving the quantitation of the cancer biomarker carcinoembryonic antigen (CEA) based on the initial slope of the binding interaction, the limit of detection worsened from 2 ng/mL in buffer to 25 ng/mL in undiluted serum due to the high serum background that varied in time.[87] Initial slope-based assays take advantage of real-time binding monitoring capabilities of high-Q sensors by fitting the first few minutes of binding data to a linear regression. Though assays based on the initial slope of the binding interaction demonstrate excellent time-to-result,[45, 87, 157] the sensitivity in complex samples can be limited by the non-specific background slope. In addition to initial-slope analysis, quantitation in biological samples can also be performed based on the net shift of the binding response after a defined sample incubation time.[87, 139] After subtracting the control ring response, the net shift represents only the specific analyte binding contribution to the overall signal. Additionally, though a departure from strictly label-free sensing, sandwich assays can be used to enhance assay specificity in complex samples by adding a secondary recognition element (Figure 5). After analyte binding during an initial primary binding step requiring incubation with a complex sample, a rinse to remove non-specific sample elements is followed by a secondary antibody introduced in buffer. Sandwich assays have been demonstrated to be highly quantitative for the detection of proteins (Figure 5A),[145] viruses,[166] and nucleic acids (Figure 5B),[137] and perhaps even more importantly, the use of a second target-specific binding event confers an extra level of selectivity to the assay that is vital for sensing in complex samples.

In some realizations of high-Q sensors, the ability to monitor each step of the assay in real time is a tremendous advantage over detection protocols based on endpoint analysis. Assays can be designed to take advantage of the large quantity of real-time binding data for more quantitative fitting of time-dependent data, directly observable quality control during the assay, and rapid kinetic analyses. The ability to observe resonance responses evolve in time during an assay provides an opportunity to catch and diagnose erroneous behaviors that often go unnoticed in endpoint assays. In addition to the initial slope methods already described, real-time binding data can be used to study desorption rates for single-nucleotide polymorphism detection,[144] to profile capture agent affinities,[156, 159] and to compare polymerization kinetics.[165] These types of real-time assays have only begun to be realized, and future pursuits will undoubtedly take advantage of these capabilities for applications in areas such as biophysical interaction screening and discovering inhibitors of specific interactions, amongst many others. Despite the multitude of uses of high-Q devices established to date, there remain a number of intriguing new applications of high-Q technologies, particularly in the area of scalable and multiplexable biomolecular analysis, that still require improvements in sensitivity, dynamic range, and detection limits, even if it is necessary to sacrifice the “label-free” moniker.

Signal enhancement techniques

The response arising from target binding to high-Q sensors can be increased through a variety of methods aimed at improving the signal-to-noise ratio. High-Q optical sensor signal enhancement can involve massive tags to increase the RI change associated with analyte binding, as well as a variety of techniques associated with photonic/plasmonic interactions and enhanced fluorescence. Beyond the use of secondary antibodies to increase specificity and augment the primary binding signal,[137, 145, 166] high-RI microbeads or nanoparticles act as large mass tags that can amplify the signal and expand the dynamic range of assays. Luchansky et al. recently demonstrated the use of ~100-nm streptavidin-conjugated beads to augment the signal arising from a two-step sandwich assay (Figure

5C).[177] By combining primary, biotinylated secondary, and bead-based assay steps, the dynamic range for protein biomarker detection was shown to expand the dynamic range to at least 6 orders of magnitude. Witzens and Hochberg also recently proposed the use of target-induced nanoparticle aggregation for ring resonator signal enhancement.[178] Based on derived time constants for optical trapping of small gold nanoparticle clusters, they estimate ~10 fM detection limits and stress the ability to take advantage of the well-established chemistry of gold surfaces. Another example of gold nanoparticle-based high-Q analyte detection involves the use of microspheres to quantitate protein adsorption to gold nanoparticles captured on an aluminum oxide membrane.[53] Though promising results have been recently demonstrated, the use of nanoparticles and other high-RI labels for signal enhancement has only begun to be explored in the context of high-Q sensors. It is likely that future signal amplification strategies will incorporate ideas from well-established enhancement strategies for SPR and fluorescent techniques. These potential strategies include rolling circle amplification,[179, 180] enzymatic amplification,[181] gold nanospheres[182, 183] and nanorods,[184] and the immuno-hybridization chain reaction.[185]

Other recent advances in signal enhancement have centered on enhanced fluorescence and quantum dot-coupled high-Q sensors. Enhanced fluorescence takes advantage of the long photon lifetimes (Equation 6) and highly localized optical intensity of WGM sensors to increase the probability of fluorophore excitation.[186] Photonic crystal enhanced fluorescence generates improved signal-to-noise for microarray-based immunoassays,[128, 132] and photonic crystal substrates can be rationally designed such that their TM and TE-polarized resonant wavelengths overlap with the fluorophore excitation and emission wavelengths, respectively. This augments the fluorescent signal-to-noise ~6× through both enhanced excitation with the localized high-intensity field as well as enhanced extraction of the emitted fluorescence. A similar principle leads to ~100× enhancement of quantum dot fluorescence emission on a 2-D photonic crystal slab engineered with leaky eigenmodes that also overlap with quantum dot excitation and emission wavelengths.[125] High-Q microspheres have also been used to excite embedded quantum dots.[61] Beyond enhanced fluorescence and quantum dot coupling, high-Q sensors could also be engineered to take advantage of non-traditional optical signals such as band-edge fringe effects in photonic crystals.[187] Further advances in signal enhancement have the potential to open doors to more demanding assays, further increasing the broad utility of high-Q optical sensors for a variety of interesting applications within chemistry, biology, and physics.

Recent Applications of High-Q Optical Sensors

The first several years of high-Q optical sensing applications generally focused on rudimentary proof-of-concept biosensing demonstrations that involved biotin/streptavidin binding or the detection of BSA physisorption to the sensor surface in buffer.[25, 39–41, 79, 82] These pioneering studies were incredibly important for demonstrating the potential of high-Q optical sensing, and excitingly, the last few years have witnessed the rapid expansion of high-Q optical demonstrations for increasingly relevant, real-world detection challenges. Recent applications have involved such important endeavors as clinically relevant measurements for in vitro diagnostics, fundamental biological studies, drug screens, exquisite light manipulation, and detailed kinetic analyses. After an extensive review of novel assays for a host of molecular classes, we describe recent applications of high-Q optical sensors for such tasks as affinity profiling, high-throughput multiplexing applications, nanoparticle transport and sizing, light manipulation and lasers, and novel uses of high-Q sensors for imaging and thermal sensing.

Biomolecular and cell-based assays

The majority of high-Q sensing applications have involved the creation of biomolecular assays for proteins and nucleic acids. Recent work in the realm of nucleic acid analysis has focused on DNA[133, 142, 144] and microRNA (miRNA)[135, 137] detection, as well as methylation analysis,[188] single-nucleotide polymorphism (SNP) discrimination,[133, 142, 144] and nucleic acid-protein interaction screens.[189] Vollmer et al. first showed the utility of high-Q microspheres for label-free DNA detection, using two microspheres of different sizes modified with two different 27-mer single-stranded (ssDNA) capture probes.[133] They were able to specifically detect 1 μM complementary ssDNA and discriminate between single nucleotide polymorphisms (SNPs). Using the LCORR system, Suter et al. demonstrate quantitative 25-mer DNA quantitation from 0.5–500 nM using the equilibrium binding shift after 15–20 min,[142] and utilized the same platform to analyze oligonucleotide methylation using both methyl-binding protein and anti-5-methylcytidine antibodies as capture agents.[188] Recent studies by Qavi et al. using microring resonator arrays demonstrate the ability to quantify 15-mer DNA across 3 orders of magnitude (nM-μM) in a 10-min assay based on the initial slope of the DNA binding curve, demonstrating a detection limit of 195 fmol of target DNA.[144] Moreover, the authors then used differential desorption rates and high stringency buffers to distinguish perfect complements from (SNPs) having variable GC contents.[144] Microring resonator arrays allow for various SNPs to be arrayed and screened to compare variable desorption rates that are indicative of binding affinity. Beyond the analysis of DNA, small (19–24 nucleotide), non-coding miRNAs that regulate gene expression at transcriptional and post-transcriptional levels are also important targets. Qavi and Bailey demonstrated the ability to simultaneously detect 4 miRNAs with DNA capture probes in 10 min with a detection limit of 150 fmol, applying the microring resonator chip to miRNA expression profiling of a glioblastoma model cell line.[135] Subsequent work with miRNAs has focused on signal amplification using an antibody specific for the DNA:RNA heteroduplex (Figure 5B), improving detection limits by 2–3 orders of magnitude to 10 pM (350 amol) in a 40-min assay.[137] Outside of WGM resonator sensors, photonic crystals have also demonstrated interesting nucleic acid sensing applications. For example, Chan et al. demonstrated the utility of replica-molded photonic crystal microwell plates for high-throughput screening of small-molecule inhibitors of protein-DNA interactions,[189] and photonic crystals were also used to characterize the DNA printing quality and uniformity of widely used cDNA microarrays.[127]

Protein analysis is another popular application of high-Q optical sensors that has received extensive attention due to the large number of protein assays used at present in the clinic. High-Q protein biosensing has largely focused on disease biomarker analysis[45, 87, 128, 139, 143, 169, 177] and cytokine profiling.[46, 132, 145, 157] An early, stimulating report of high-Q protein analysis by Armani et al. described the use of a silica microtoroid for label-free detection of the cytokine interleukin-2 (IL-2) in undiluted serum with single-molecule sensitivity.[42] This unprecedented sensitivity was attributed to the thermo-optic effect, which was claimed to result in a quadratic dependence of sensitivity on the Q factor (10^8) as bound IL-2 causes an increase in the local temperature of the microtoroid. However, recent theoretical studies by Arnold et al. contest these results by asserting that the thermo-optic enhancement mechanism is dwarfed in magnitude by the well-understood reactive mechanism associated with binding-induced RI changes.[190] Arnold went on to show that the thermo-optic effect can account for no more than 0.1% of the wavelength shift magnitude associated with single-molecule binding events. Despite the controversial nature of this single-protein detection paper,[42] it has generated significant interest, activity, and conversation within the high-Q biosensing community. Many researchers in the field are anxiously awaiting follow-up reports that would help to robustly establish fundamental limits of high-Q sensors, particularly for applications in complex matrices where single

molecule binding events would almost certainly be difficult to observe independent of competition with non-specific binding.

In other protein detection work, Washburn et al. demonstrated the ability to detect the cancer biomarker carcinoembryonic antigen (CEA) at clinically relevant concentrations using an array of SOI microring resonators.[87] This CEA assay, based on initial slope-based quantitation performed in just 5 min, yielded a limit of detection of 2 ng/mL in buffer, comparable to a commercial ELISA, and CEA was also detected in undiluted fetal bovine serum, albeit with a less impressive detection limit (25 ng/mL). Zhu et al. used the LCORR system to detect the cancer biomarker CA15-3 in diluted serum samples from stage IV breast cancer patients, with a detection limit of ~20 units/mL (~1 unit/mL in buffer) for a 30-min equilibrium shift assay.[139] Healthy samples were differentiated from cancer patient samples, and CA15-3 levels agreed well with pathology test results. Gohring et al. also used the LCORR system to demonstrate detection of the breast cancer biomarker HER2 between 13 and 100 ng/mL in serum based on a similar 30-min equilibrium shift assay.[143] Multiplexed protein biomarker detection has also been demonstrated, with Washburn et al. showing the simultaneous quantitation of 5 cancer biomarkers (CEA, alphafetoprotein [AFP], prostate specific antigen [PSA], tumor necrosis factor-α [TNFα], and interleukin-8 [IL-8]) from the same solution using 5-min initial slope analysis on microring resonators.[45] Though this initial multiplexed biomarker assay was performed in buffer, it demonstrates the ability to design useful assays for multiple proteins with limited cross-reactivity and no loss of sensitivity or precision in the extension beyond single-parameter assays. Current protein biomarker efforts have centered on improving sensitivity and dynamic range in the analysis of clinical samples, and a recent report showed the ability to detect the cardiac biomarker C-reactive protein (CRP) in diluted human serum and plasma samples across six orders of magnitude of dynamic range with a limit of detection of 30 pg/mL.[177]

Beyond protein biomarker assays, cytokines represent an even more challenging target due to their small size (5–40 kDa)[191] and low relevant concentrations (pg/mL-ng/mL).[192] Luchansky and Bailey demonstrated the ability to detect the cytokine IL-2 down to 100 pg/mL (6 pM) in buffer with a 45-min sandwich immunoassay performed on microring resonators (Figure 5A), and this assay was applied to IL-2 temporal secretion analysis of Jurkat T cells.[145] More recently, the same authors developed a method for extremely rapid, multiplexed cytokine (IL-2, IL-4, IL-5, TNFα) analysis based on 5-min initial slope quantitation of one-step sandwich assays on a ring resonator chip.[157] This multiplexed cytokine platform can be applied to immunological studies with improved temporal resolution, showing the ability to discriminate differentiated primary T cell lineages based on their cytokine secretion profiles. Also focusing on cytokines, Mandal et al. used 1-D photonic crystal sensors for the multiplexed detection of IL-4, IL-6, and IL-8 at concentrations >1 μg/mL with two-step sandwich assays.[46] Other work with replica-molded photonic crystal sensors has focused on using enhanced fluorescence for improved performance and augmented signal-to-noise in fluorescent protein microarrays for both cancer biomarkers[128] and cytokines.[132]

Interesting high-Q sensor applications have also emerged in the area of cell and particle analysis, including bacteria,[54, 76] T cell,[193] and virus detection,[56, 57, 166, 176, 194] as well as studies that analyze cell growth[170] and cellular processes such as apoptosis and activation.[17] Microorganisms were first detected with microspheres by Ren et al., who observed random adsorption of rod-shaped *E. coli* bacteria cells and the accompanying decrease in Q factor caused by increased scattering losses.[54] Ramachandran et al. later demonstrated the use of high-RI glass microring resonators for specific capture of *E. coli* cells only on rings coated with anti-lipopolysaccharide, with a detection limit of 10^5 colony-forming units (CFU)/mL.[76] Human $CD4^+$ and $CD8^+$ T cells at concentrations as low as 2×10^5 cells/mL were

also detected with optofluidic ring resonators, albeit with limited dynamic range.[193] Virus detection has also been achieved with microsphere,[56, 57] microtoroid,[176] microring,[194] and optofluidic resonators.[166] Zhu et al. detected the bacteriophage M13 at concentrations down to 10^3 plaque-forming units (PFU)/mL using optofluidic resonators,[166] and Vollmer et al. demonstrated single-virus detection of ~100-nm Influenza A particles with spherical microcavity resonators.[56] In the latter report, microsphere sensitivity to viral particle binding was also observed to increase with decreasing microsphere size (and accompanying increase in radius of curvature) that leads to greater wavelength shift per bound particle. Lu et al. also recently reported single-virus detection of Influenza A particles by adsorption to microtoroids.[176] They utilize a thermal-stabilized reference interferometer to minimize noise associated with laser frequency jitter and scan-voltage control, achieving an incredible 0.1 fm wavelength shift resolution. McClellan and Bailey recently utilized microring resonator arrays for an agricultural application of virus detection, demonstrating the quantitative analysis of bean pod mottle virus particles from minimally-processed in leaf extracts.[194]

Beyond quantitation of cell and particle binding to WGM sensors, high-Q sensors can also be used for monitoring cellular processes. Wang et al. demonstrated the ability to use microring resonators to observe cell growth, cellular adhesion processes, and cellular response to toxins.[170] By attaching MS1 endothelial cells to the microrings, changes in cell volume and motility led to RI perturbations that allowed for on-chip cell proliferation monitoring after seeding. They also demonstrated the ability to detect cellular toxins at relevant levels based on the root mean square (RMS) of resonance wavelength fluctuations that varies with cell viability. In recent work, Wilson et al. used fibronectin-coated microspheres to culture neurons and skeletal myoblasts and to study the effects of surface adsorption on cellular function.[195] Beyond the analysis of whole-cell attachment, a biomimetic coating composed of a lipid bilayer has been self-assembled on microspheres by Freeman et al.[196] This could provide a useful model of the cell membrane for monitoring processes such as membrane transport. Photonic crystals, most notably incorporated into a microplate format, have also been used for a wide array of cell-based assays based on either aggregate cell behavior or single-cell measurements. Recent progress in this area, including applications to studies of cell attachment, cytotoxicity, apoptosis, GPCR activation, ion channel activation, and chemotaxis, have been nicely reviewed.[17] Though ensemble measurements of aggregate cell behavior have been widely reported, label-free photonic crystal imaging[197] has been developed to study cell attachment distribution within individual cells with a pixel resolution of $<1\ \mu m^2$.[198] By coating photonic crystal sensors with proteins that model the extracellular matrix (ECM), Lidstone et al. use photonic crystal enhanced microscopy (PCEM) to study cell adhesion during growth, apoptosis, and differentiation processes (Figure 6).[198] Without the need for fluorescent labels, PCEM permits increased cell viability for long-term studies of the same cells. This new imaging technique could provide important insights into cell-ECM interactions that are vital in processes such as wound healing and cancer metastasis.

Chemical assays: Vapor-phase sensing, reaction monitoring, and molecular orientation

Beyond aqueous biomolecular assays that have received a large amount of attention from the high-Q sensor community, applications in chemical analysis have also been reported–applications such as detecting gases[106–108, 130, 154, 155, 199, 200] and vapor-phase explosives,[151, 152] studying thin films[201] and polymer growth,[3, 46, 165] and discriminating chirality,[202] photoisomerization,[203] and molecular orientation.[204] High-Q devices have demonstrated vapor-phase sensing applications such as acetylene sensing with slotted microring resonators,[199] microsphere analysis of He/Ar mixtures based on changes in gas thermal conductivity,[200] ethanol vapor sensing with ZnO nanoparticle-coated racetrack microring resonators,[154] and hydrogen sensing based on combustion at a Pt/WO_3 catalyst-

coated microring.[155] Gas detection methodology was described in the surface chemistry section, and the most important applications have centered on gas chromatography (GC) detectors and explosives detection for security applications. Optofluidic ring resonators have emerged as an extremely promising platform for GC detection that combines WGM optical interrogation with a stationary-phase coating for vapor-phase separation.[106–108] In another use of an optofluidic resonator, Sun et al. demonstrated the specific detection of DNT at room temperature from a nitrotoluene background with a 200 pg limit of detection.[151] Similarly, Orghici et al. used microring resonators to demonstrate specific vapor-phase detection of TNT at concentrations down to 1 ppb, though the dynamic range of the analysis was limited to a factor of 10.[152] Though tools such as GC-MS remain more sensitive, high-Q sensors have yet to be fully realized for these gas sensing applications and thus represent a promising platform for portable detection systems.

Other chemical assays have centered on real-time reaction monitoring, especially in the realm of polymer chemistry. Real-time analysis of surface chemistry functionalization, capture agent immobilization, and assay monitoring has been described in previous sections, but the ability to monitor surface-based changes in real-time is also useful for polymeric processes. High-Q sensors have demonstrated the ability to monitor polymer electrolyte multilayering,[3, 46] observe temperature-induced changes in optical properties (i.e. RI) of polymer thin films,[201] and compare atom transfer radical polymerization growth processes under different catalytic reaction conditions.[165] Due to the high temporal resolution, potential for parallel screening of reaction conditions, and label-free operation, high-Q optical sensors are extremely promising for reaction monitoring, and the potential of these technologies has only begun to be realized in this arena.

In addition to polymer applications, properties such as chirality and molecular orientation can also be probed with WGM sensors. Vollmer et al. showed that a ring resonator can be used to observe the circular birefringence of a chiral liquid based on the relative wavelength position of optical modes associated with left and right circularly polarized light.[202] Specifically, the variation in splitting of left and right circularly polarized modes was shown to be a function of the enantiomeric excess of the optically active liquids. Beyond studying chirality, molecular orientation on a surface can also be studied with WGM sensors. Topolancik et al. demonstrated the ability to observe photoinduced isomerization transformations of a bacteriorhodopsin (bR) layer adsorbed to a poly(dimethyldiallyl)ammoniumchloride–coated microsphere.[203] They utilize time-resolved switching data to probe the polarization transformations that accompany the *cis*/*trans* isomerization of the retinal chromophore within bR. Specifically, polarization transformations were observed by measuring the shift ratio of the TM- and TE-polarized WGMs. A similar TM/TE WGM shift ratio technique can also be used to probe the orientation of BSA on a silanized microsphere.[204] Though these studies demonstrate truly innovative uses of WGM sensors, additional follow-up studies will be required to extend these findings to the study of molecular orientation within additional protein systems.

Multiplexed measurements: Screening, kinetic analysis, and affinity profiling

Beyond the demonstration of interesting applications for chemical and biomolecular sensing, multiplexed assay techniques must be developed in parallel to leverage the scalability of high-Q geometries such as microring resonators and photonic crystal sensors. Arrays of microring resonators have become a valuable tool for efficient parallel screening of capture agent affinities, allowing direct comparison of association and dissociation rates.[156, 159] Once a high-Q sensing platform has been established, the first (and often rate-limiting) step in developing a new assay is the search for effective capture agents, such as an antibodies or aptamers. SOI microring resonators have shown the ability to screen several capture antibodies in parallel based on DNA-encoded antibody technology (Figure 7A),[159] and the

ring resonator array platform has also been used to directly assess the relative utility of antibodies and aptamers for a common target.[156] By providing real-time kinetic analysis of target binding to potential capture agents, the optimal antibody or aptamer can be chosen based on direct comparison of important physical properties such as association and dissociation rate constants, robustness, reproducibility after regeneration, specificity, and suitability to amplification steps such as sandwich assays. Importantly, information about capture agents gained on scalable high-Q platforms is useful not only in assays performed on the same platform, but also for a host of fluorescent, enzymatic, plasmonic or electrochemical assays carried out with a variety of alternative transduction modalities techniques. After careful selection of a capture agent, microring resonators also permit multiplexed assays of proteins[45, 97, 98, 157] and nucleic acids,[135, 137] as described in previous sections. Some of these assays also make use of fast, kinetic-based quantitation based on initial-slope analysis,[45, 87, 157, 177] which further showcases the importance of real-time binding capabilities of many high-Q devices. For example, multiplexed, initial-slope based quantitation has found an interesting application in monitoring cellular secretion of cytokines (Figure 7B).[157] Finally, another sensing methodology that could eventually be amenable to high-level multiplexing involves optical spectroscopy in 200-μm silicon nitride ring resonator cavities.[205] Within a ~100-fL reaction volume enclosed by the ring resonator, changes in optical absorbance lead to resonant wavelength shifts that are not dependent on thermal fluctuations. This concept could be extended to perform fast ELISA-type absorbance assays in very small volumes with inherently multiplexable microring resonators. Continued development of ring resonator technology will continue to take advantage of the inherent scalability of planar silicon-based devices, and arrays of hundreds of sensors on a chip are in sight.

Multiplexed assays have also been developed based on 1-D photonic crystals[46] and photonic crystal microplate devices.[121, 148, 173, 189] Beyond the 1-D photonic crystal fluidic devices already discussed,[6, 46] the ability to interface photonic sensors with plastic 96- or 384-well plates (Figure 7C) represents an important development for label-free, high-throughput screening applications. Photonic crystal sheet biosensors have been used to screen small-molecule modulators of protein-protein interactions (Figure 7D),[148] to discover inhibitors of protein-DNA interactions,[189] and to analyze biomolecular binding kinetics.[121] Applications such as these require excellent sensor uniformity on low-cost substrates that are compatible with automated fluid handling robotics. A recent extension of replica-molded photonic crystal substrates is the creation of distributed feedback laser biosensors (DFBLB).[206] The DFBLB system achieves Q factors of 10^4–10^5 through stimulated emission from a rhodamine dye-doped SU-8 layer over a periodic polymer grating, allowing any area of the substrate to act as a sensor without rigorous alignment requirements. These sensors can be fabricated by standard roll-to-roll manufacturing. As developments in fabrication techniques continue and new applications emerge, photonic crystals will remain important for multiplexed studies involving screening, detection, and imaging.

Nanoparticle analysis and optical manipulation

The impact of high-Q optical sensors on nanotechnology has expanded in recent years, with novel examples of nanoparticle detection,[56, 109, 176, 207–209] sizing,[56, 210, 211] sorting,[96, 210] and optical manipulation.[212–215] Vollmer et al. first showed single particle detection of 500-nm polystyrene spheres using 90-μM WGM microsphere resonators.[56] Discrete wavelength shifts accompanying single-particle binding events were clearly resolved. Recent experiments by Lu et al. demonstrated the ability to detect single-particle binding of much smaller 25-nm polystyrene particles, observed as a 0.4±0.2 fm resonance wavelength shift on a thermally-stabilized microtoroid resonator.[176] Single-particle binding is accompanied by both a longer WGM pathlength (and corresponding shift to longer resonance wavelength)

as well as an increase in backscattering, which work together to create a measurable binding signal. Vollmer and Arnold describe an important optical trapping mechanism, dubbed the WGM carousel, that is responsible for attraction and subsequent orbiting of particles at the region of highest evanescent intensity in microsphere devices.[216] Though nanoparticles in solution are governed by Brownian motion, nanoparticles are drawn toward the resonator surface by attractive opto-mechanical gradient forces similar to those employed by optical tweezers.[57] Due to this opto-mechanical force, the nanoparticle binding timescale in very dilute solutions (aM or less concentrations) is sped up well beyond that predicted by the theoretical diffusive or convective binding models.[171] The WGM carousel force is a function of the device Q factor (Equation 5) and laser power, drawing the nanoparticles toward the highest intensity of the decaying WGM evanescent field at the microsphere equator surface. Once particles are held in orbit near the surface by a combination of optical forces and interfacial interactions, the probability of particle binding approaches unity.[57, 216] These optical trapping forces are helpful for detection of particles at low concentrations, and they may find utility in a number of high-Q detection strategies.

In theoretical work describing modified microbubble or microbottle optofluidic ring resonator geometries, Li et al. showed that the three-dimensionally confined fluidic path should improve the sensitivity for nanoparticle detection beyond that of traditional microspheres by an order of magnitude.[207] By optimizing capillary wall thickness and bubble curvature, modified optofluidic resonators should permit detection of sub-40-nm nanoparticles. In addition to sphere, toroid, and optofluidic geometries, single-nanoparticle detection has also been proposed based on using the gap area in a system of two microdisk resonators, and finite difference time domain models suggest that the sensitivity should increase with both decreasing gap size between the disks as well as increasing microdisk thickness.[208] Other examples of nanoparticle detection by Koch et al. involve the previously described hurricane geometry for 100-nm gold nanoparticle detection[109] as well as reflection-mode sensing based on nanoparticle-induced backscattering in an add/drop filter microring device.[112] The reflection-mode sensor is based on reflection from a bound nanoparticle that causes light to circulate the cavity in the opposite direction, leading to an intensity build-up of backward propagating modes that can be detected with a broadband detector. Though most nanoparticle detection platforms are based on a red shift to longer resonance wavelengths, consistent with an increase in the local RI, it is also possible to detect nanoparticle binding through a negative or blue shift in the resonance wavelength.[209] On account of the unusual optical properties of gold nanoparticles, a blue shift in the resonance wavelength during binding to a microring in air was observed and explained to be the result of the smaller real component and large imaginary component of the RI for gold relative to air in the near IR spectral region. This “negative” signal differentiates gold nanoparticle binding from dielectric particle (biomolecules, polymers, etc) binding, which could lead to interesting methods to circumvent signal-to-noise limitations in high-background matrices. It should also be noted that metallic nanoparticles degrade the WGM resonance through scattering losses, leading to a broadening of the resonance wavelength peak and thus reduced spectral resolution.

Beyond nanoparticle detection, WGM sensors also enable nanoparticle sizing and sorting. In addition to the proportionality of the discrete wavelength shift to the particle size/mass,[56] particles can also be sized or “weighed” through mode splitting. Zhu et al. show that the deposition of single nanoparticles as small as 60 nm to a high-Q microtoroid leads to splitting of the WGM into two spectrally shifted resonance modes (i.e. a doublet).[210] Nanoparticle deposition causes scattering that breaks the perfect azimuthal symmetry in the microtoroid, lifting the degeneracy in the WGM modes that propagate in opposite (clockwise and counterclockwise) directions in the toroid (Figure 8). This phenomenon allows for the sizing of both KCl and polystyrene nanoparticles (60–350 nm) based on the

accompanying normalized magnitude of the WGM splitting.[210] A benefit of mode splitting analysis is that mode splitting is independent of nanoparticle position on the resonator, an advantage over shift analysis that depends on where on the high-Q structure the particle resides. In addition to splitting-based sorting of nanoparticles on the basis of size, nanoparticles can also be sorted based on their composition. Notched ring resonators, which contain a ~100-nm notch fabricated by e-beam lithography, feature an area within the core of the waveguide with a strong (non-evanescent) electromagnetic field that greatly enhances the optical interaction with a nanoparticle within the notch.[96] Nanoparticle binding, simulated by a 20-nm nanoparticle AFM tip placed in the notch, caused large (nm-scale) resonant wavelength shifts. Easily discernible shift and splitting behaviors for both silicon and gold particles have been proposed, although not yet realized, as a way to sort nanoparticles of differing compositions. A final innovative method for nanoparticle sizing involves the interrogation of nanoparticle Brownian motion as it relates to WGM resonance wavelength fluctuations.[211] Virus-sized nanoparticles near a microsphere cause “noise” in the resonant wavelength based on stochastic processes associated with Brownian motion, which was well-characterized by an autocorrelation function. The normalized autocorrelation of resonance wavelength fluctuations provides a good estimate of nanoparticle size, especially for nanoparticles less than 100 nm in diameter.

Beyond detection and characterization applications, WGM resonators can also be used to manipulate the motion of particles. For example, Yang and Erickson recently created an optical switch by using a 200-μm SU-8 polymer ring resonator to trap and manipulate particles.[212] By switching between on- and off-resonance wavelengths inserted into the bus waveguide, the motion and position of 3-μm polystyrene particles was controlled; particles trapped on the bus waveguide could be routed to the microring by on-resonance wavelengths that caused a build-up of the optical-trapping WGM carousel forces (Figure 9A). Similar work by Cai and Poon demonstrated optical transport and manipulation of slightly smaller 1-μm polystyrene particles on a silicon nitride microring platform.[213] They used the optical trapping effects to create a particle add-drop filter device (with both a throughput/input and a drop/output waveguide) that functions as a type of “particle circuit.” Lin et al. used smaller 5- and 10-μm silicon microring resonators (Figure 9B) and 200 frame/s videos to measure the particle velocity (~10^{-4} m/s) and revolution frequency (~3Hz) of similar fluorescent ~1-μm polystyrene particles.[214] Particle trapping in the ring required only 0.67 mW of optical power, and particle revolutions were stable for several minutes. Finite-difference time-domain (FDTD) studies show that the electromagnetic field intensity on top of the small microrings follows a Gaussian distribution (Figure 9C). Interestingly, the particles were observed to slow at the far end of the microring distal to the bus waveguide, likely due to bending-loss induced attenuation of the field enhancement. Impressively, Mandal et al. demonstrated the ability to statically trap smaller 48- and 62-nm polystyrene particles with 1-D silicon photonic crystals.[215] The photonic crystal device allows optical trapping capabilities beyond those of traditional optical tweezers, and this device could permit applications in particle trapping, storing, and sorting independent of microfluidic flow. Various optically trapping photonic crystal geometries have been characterized, and comparison of trapping stiffness and stability for different geometries allows for optimization of field enhancement and confinement.[217] In addition to the potential benefits of the high-Q optical trapping approach for single-molecule manipulation, nanomanipulation of this type also holds promise for bottom-up nanomaterials synthesis by directed assembly.

Microcavity and photonic crystal lasers

Outside of passive microcavity sensing, another interesting application of high-Q devices is the development of microcavity and photonic crystal lasers. Although not the focus of this review, there are several historical examples of improved laser designs significantly

impacting analytical detection methodologies, and thus the subject is covered here in brief. Compact, single-mode, low-threshold (4 mA) lasing was demonstrated with 50-μm hybrid devices composed of InAlGaAs/InP microrings on a SOI microdisk (Figure 10A). These devices were proposed for use as on-chip optical interconnects.[218] Further reductions in device size and increases in facet reflectivity will likely lead to further reductions of lasing thresholds (Figure 10B). Though lasing from a microcavity device is non-directional due to the cavity's radial symmetry, highly unidirectional lasing is possible from a high-Q WGM based on incorporation of a wavelength-scale notch at the boundary of an elliptical quantum cavity laser.[219] Single-mode lasers can also be formed based on coupled microcavities. A single-mode coupled cavity laser, formed from 2 adjacent ~100-μm silica microrings of slightly different sizes, has been demonstrated by Li et al. as a biosensor for monitoring biomolecule-induced coupling changes that alter laser light intensity.[220] Based on the Vernier effect where light from a resonant cavity is lost to the adjacent nonresonant cavity,[221] RI change-induced mode hopping allows for sensing based on the cavity laser intensity measured by a spectrometer (rather than monitoring the resonance wavelength shift). A similar single-mode coupled optofluidic device, which also uses the Vernier effect to suppress unwanted side modes, has been created in replica-molded PDMS, thus potentially allowing for simple mass production.[222] Another interesting optofluidic cavity device, developed by Sun et al., is a dye laser in which an optical fiber is fused to the inner wall of the microcapillary ($Q = 10^5–10^6$), which permits fluidic control of the rhodamine 6G dye-based gain media.[223] Optofluidic dye lasers can also be excited by DNA scaffold-controlled FRET interactions.[224] Photonic crystal lasing has also been demonstrated with a GaAs photonic crystal waveguide[225] and a 2-D GaInAsP slab with a 30-nm nanoslot lattice discontinuity.[226] The GaAs photonic crystal waveguide laser features spatial localization of various lasing modes along the waveguide, while the nanoslot discontinuity leads to high laser localization within the slot for possible sensing applications. Though microlasers tend to have smaller photon numbers and broader mode linewidth than traditional (larger) lasers,[21] microlasers benefit from small mode volume and low lasing thresholds. Recent progress in the development of silicon lasers[227] and rare earth ion-doped microsphere lasers[16] have been recently reviewed.

Thermal sensing

Temperature-induced resonance wavelength fluctuations were discussed earlier as a limitation of high-Q devices, requiring careful temperature control or on-chip referencing to prevent thermal noise-limited sensing. However, the high temperature sensitivity of high-Q devices can also be advantageously harnessed for accurate, small-footprint thermal sensing. As described earlier, WGM microcavities were used for analysis of thermal-induced changes to polymer thin films in hybrid silicon-polymer devices.[201] Kim et al. demonstrated and quantified the strong impact of temperature changes on the resonance wavelength in silicon microrings owing to the thermo-optic effect, observing a thermal sensitivity of 82 pm/°C.[228] The 8-μm ring resonator thermal sensor displayed an impressive 6-μs response speed, and the small ring dimensions led to an improved FSR that was associated with a broad dynamic range of ~300 °C. By incorporating a 2.25-μm PDMS thin film on a silica microtoroid, superior temperature sensitivity of 151 pm/°C and resolution of 10^{-4} °C was reported.[229] For thicker PDMS films, the negative thermo-optic coefficient of PDMS dominates the positive coefficient of Si, leading to a blue shift in resonance wavelength with increasing temperature. Based on their high thermal sensitivity and low response times, arrays of WGM resonators may one day function as high-spatial density thermal detectors for high-performance thermal imaging.[230] Watts et al. showed that silicon nitride microring resonator thermal detectors (Figure 10C) are sensitive to thermally induced changes caused by an incident CO_2 laser beam, demonstrating excellent response time and temporal resolution (Figure 10D). For room-temperature thermal imaging, the advantages of high-Q

structures over cryogenically cooled devices are expected to include lower thermal noise, smaller pixel size, lower response time, and high inherent scalability.[230] Many-element (10^2–10^3) arrays of photonic sensors are currently being developed for multiplexed sensing applications, but thermal imaging applications should further drive scalability of integrated devices due to their requirement for an array of $>10^6$ sensors.

Other applications: Ultrasonic detectors, spectral imaging, and integration with other techniques

Microcavity devices have also found utility in other detection and imaging applications. Beyond the ability to act as a detector of RI changes, molecular binding, and temperature, microring resonators can function as ultrasonic detectors. Ninety μm polymer microrings fabricated from thermally reflowed resist molds, as described earlier, have smooth sidewalls and demonstrate high Q factors of 10^5, allowing for 36.3 mV/kPa acoustic sensitivity.[90] For ultrasonic imaging applications, this high acoustic sensitivity on a small footprint is very desirable. Low noise at high frequencies is another important attribute of ultrasonic detectors, and these polymeric microrings demonstrated a pressure noise floor of 88 Pa in a 1–75 MHz bandwidth range, which is substantially better than piezoelectric transducers of similar size and bandwidth. Further work by Ling et al. has demonstrated similar noise levels and Q factors on a smaller footprint (60-μm polystyrene microrings) by shifting the working wavelength from the near-IR to 780 nm to reduce water and polymer absorption.[83]

High-Q devices can also be used as polarization-sensitive IR detectors. Rosenberg et al. showed that a metal-coated dots-in-a-well (DWELL) photonic crystal cavity can be designed to achieve significant free-space coupling of normal-incident light.[231] Additionally, Boriskina et al. show that the large confinement of high-Q cavities could be combined with the superior light concentrating properties of nanoantennas to create optoplasmonic superlenses for low-loss energy transfer within optical circuits.[232] The proposed superlens is composed of a polystyrene microsphere sandwiched between two gold nanodimer antennas, creating a device that is well suited for frequency-sensitive enhancement and switching of light at the nanoscale. Regardless of the application, high-Q optical detectors benefit from multi-pass interactions, large optical confinement, scalability, and high sensor spatial density.

Beyond detector applications, additional uses of high-Q technology may be enabled through integration of microring resonators with other photonic devices including interferometers and Bragg reflectors. High-Q Mach-Zehnder interferometer (MZI)-coupled silicon microrings have been demonstrated with Q factors as high as 10^5–10^6.[233] By adjusting the relative lengths of the arms of the MZI coupler to carefully select the interference order, it is possible to depress all except for one resonant wavelength. This leads to an unusually large FSR (up to 180 nm), which allows for sensing over a broad RI range of up to 0.5 RIU. Numerical simulations have also shown that a MZI-coupled microring has up to 30% greater sensitivity than a traditional microring of the same size and material while using 25% less circulating power.[234] These types of MZI-coupled improvements are not drastic and may not justify the extra design complexity for sensing applications, but the potential for a very large FSR could be useful for applications involving extreme RI shifts, such as those requiring sensing in both liquid and gas environments. In addition to sandwiching a microring between the arms of a MZI as described above,[233] it is also possible to create a dual-microring-resonator interference sensor that features two ~1-μm microrings of slightly different sizes, with one on both arms of a MZI.[235] In this design, the output transmission spectrum depends on the interference overlap of the two microring spectra, demonstrating improved sensitivity but a small FSR. Outside of MZI-coupled microrings, distributed Bragg reflectors on microring resonators (DBR-MRR) have been used to create a single-wavelength microring mirror. After laying out design parameters and suggesting

applications in the area of compact tunable lasers,[236] DBR-MRR designs were realized by removing 50 nm^2 sections from the inward side of the half of a 30-μm Si_3N_4/SiO_2 microring distal to the bus waveguide.[237] By only covering half of the microring with the DBR, reflectivity nulls coincide with all resonant wavelengths save one,[238] leaving only one reflected resonance wavelength, which is the basis for a single-wavelength mirror that features 92% peak-power reflectivity.[237] The integrated device could be used as an in-line mirror for low-threshold, narrow linewidth single mode laser diodes. Though many applications of integrated optical devices have been demonstrated, only a few were chosen as representative of interesting recent examples of microring resonator-integrated devices. High-Q devices in optical communications applications, such as filtering, modulating, switching, routing, and delaying, has been recently reviewed.[9] While it is clear that the use of high-Q optical devices for biosensing and other analytical applications has become a vibrant research community in itself, it is important to be cognizant of the massive amount of effort that has been invested in applying high-Q devices to fundamental optics and telecommunications applications.

Perspectives

Summary of recent advances and areas of needed improvement

A multitude of advances in high-Q sensing have been realized in the last few years. Though most of the high-Q geometries in use today have been around in some form for at least the better part of a decade, exciting recent improvements include new geometric architectures, novel fabrication techniques and material systems, innovative methods for improving device quality and scalability, and increased control and robustness of optical interrogation. Beyond fabrication considerations, surface chemistry and functionalization strategies have both evolved to include reproducible, covalent sensor modification, effective non-fouling modifications and blocking strategies, and surface regeneration methods. Once functionalized with appropriate capture agents, high-Q sensors have been used in a variety of increasingly well-developed assays, as described at length earlier. Key assay developments of the past few years include advances such as on-chip thermal referencing, the creation of robust microcavity interrogation hardware, improved signal quantitation and calibration methods, integration of microfluidic sample handling, and the realization of multiplexed sensing. The development of increasingly complex assays in relevant sample matrices has also been aided by a variety of new strategies aimed at improving specificity and boosting signal-to-noise for trace analysis. All of these advances in fabrication, surface chemistry, and assay methodology have enabled the wealth of new applications of high-Q sensing that have emerged in the past few years. Important recent applications range from multiplexed protein assays to vapor-phase explosives analysis, from single nanoparticle analysis to WGM carousel optical manipulation, and from miniature high-Q lasers to sensitive ultrasonic and thermal detectors.

Despite the successes, improvements are still needed on several fronts in order for the ultimate potential of these technologies to be realized. Though excellent quality factors have been reported for a variety of geometries, the noise floor in relevant assays is often based on non-specific binding, not spectroscopic resolution. Put another way, the community is rapidly approaching, if it has not already reached, the situation where the optics are no longer the limiting factor. To combat and circumvent non-specific binding and surface fouling, improved surface chemistry and added levels of assay specificity must be realized. Though PEG layers and effective surface blocking have been helpful, sensing in very complex media such as human serum remains a challenge to all surface-based biosensing techniques, regardless of transduction modality. Beyond surface fouling considerations, the ultimate sensitivity of many assays is also limited by the ability to find suitable capture agents. Antibodies are notoriously difficult and time-consuming to produce and optimize

beyond nM (or at best pM) binding affinities (K_D). As assays develop that permit high-level multiplexing, the requirements for high-affinity capture agents with little or no cross-reactivity increase dramatically, and highly selective sandwich assays additionally require a pair of high-affinity antibodies for each target. Though progress has been made in creating alternative capture agents,[239–241] their affinity, robustness, and/or specificity will increasingly limit high-Q assays as more demanding analytical challenges are attempted. If the field is to progress at a rapid rate commensurate with the promise of the high-Q technologies themselves, researchers must increasingly take on real-world analytical challenges. Reports featuring detection of model proteins in buffer need to be left behind in favor of demonstrations of sensing in relevant and useful matrices such as environmental samples, cell culture media, and clinical samples. Though progress is beginning to be made in this area, the future of the field rests in realizing truly novel applications of high-Q sensing technologies aimed at elucidating fundamental biological processes, creating clinically viable platforms for development of personalized diagnostics, monitoring and/or comparing reaction conditions for catalytic processes, characterizing and sorting nanomaterials, and imaging cellular, thermal, and acoustic processes. To achieve some of these highly useful applications, additional specifics about some of the most important goals and challenges are presented below.

Future goals and challenges for high-Q sensors

Some of the main goals of high-Q sensing include integrated sensor systems, high-level multiplexing, fundamental biological studies, and high-throughput clinical diagnostics. The challenges associated with each of these goals, in our opinion, are defined below:

1. *Integrated sensor systems.* In order to achieve widespread use outside the academic lab, many aspects of large-scale systems integration must be considered, including the development of robust instrumentation that features facile optical coupling to the photonic microstructures, integration with automated fluidic handling, and customizable data processing capabilities. For many of the most promising applications, high-Q optical devices will need to reach their potential for cost-effective mass production by leveraging semiconductor processing methods, rapid prototyping, or roll-to-roll fabrication approaches. Since developing assays is a challenge in and of itself, the optics, device fabrication, and engineering work for the accompanying instrumentation can be addressed separately but in consultation with end users who have specific applications and particular specifications in mind. The challenges associated with creating a truly useful, well-packaged, and versatile high-Q sensor analytical platform are significant but attainable. Progress in this area requires broad expertise in optical engineering, device design, and assay/method development, which means that effective, multidisciplinary collaboration will be vital.

2. *High-level multiplexing.* Multiplexed assays are desirable for many applications that require high information content and fast sample throughput. Scalable geometries such as planar microrings and photonic crystal sheets appear at present to offer the highest potential for creating the multiplexed sensing platform necessary for many interesting applications such as clinical diagnostics, drug screening, and environmental monitoring. The ability to perform multiple simultaneous assays on the same sample demands the fabrication of many sensors on a small footprint. This requirement seems, at present, to be a limiting factor for many of the demonstrated non-planar geometries, such as microspheres and microtoroids that require particularly onerous optical fiber alignment. However, this is an active area of research and innovative solutions may overcome this limitation. Another engineering consideration is the capability to reproducibly

determine the resonance wavelength for each element in a multiplexed sensor array with a sufficient repetition rate to achieve acceptable temporal resolution for a given analytical challenge. Additionally, multiplexed assay methodologies, regardless of transduction modality, face considerable challenges associated with capture agent availability, specificity, and cross-reactivity, as outlined earlier. Many multiplexed detection strategies also observe reduced sensitivity compared to corresponding single-parameter assays because the multiplexing is complicated by the inability to individually optimize the assay for each target within a panel. Furthermore, analyte concentrations vary widely both from one sample to the next and also vary among different analytes in the same sample. This means that assays and sensors with broad dynamic ranges will be needed to prevent multiple time-consuming dilutions. Photonic crystal sensors have been quite successful in several of these regards and should serve as a model for the development of alternative high-Q sensing platforms.

3. *Fundamental biological studies.* In order to harness advances in systems integration and high-level multiplexing, researchers should seek out systems in which insights into fundamental questions are considerably easier to answer with the scalability and real-time analysis capabilities of high-Q sensors. Although single-molecule studies have been suggested, results of this kind may not be feasible in complex environments. Nonetheless, high-Q sensors have demonstrated requisite sensitivity for many applications of contemporary importance. Some of these applications, among many others, include screening modulators of protein-protein interactions, analyzing binding kinetics, and monitoring cellular secretion processes. The movement away from proof-of-concept experiments will require well-validated assays that can be similarly robust, but more informative, than currently available competitive technologies. The extension of high-Q sensors to fundamental biological studies will be facilitated by collaborations between scientists from varied disciplines so that expertise in biological systems can be combined with the wealth of sensor development and quantitative analysis expertise that is already present in the high-Q sensing community.

4. *High-throughput clinical diagnostics and environmental monitoring.* Some of the most important areas that require effective collaborations are those for which patient or environmental samples will need to be analyzed. By forging interdisciplinary collaborations, the quantitative analysis and method design capabilities of analytical chemists can be combined with deep knowledge and expertise of a particular subject as well as access to interesting samples. In these areas, large numbers of samples need to be run via standard assay protocols in order to establish a conclusion, again requiring robust instrumental platforms. Additionally, it seems that many of the most interesting applications generally require high sensitivity in a challenging sample matrix. For this reason, researchers must continue to investigate new strategies for increasing the signal-to-noise ratio for complex analyses—a feat that will likely involve signal amplification, surface chemical optimization, and perhaps sample pre-treatment methods. Effective capture agents, either natural or artificial, will also need to be developed, and multidisciplinary collaborations involving synthetic chemists, biochemists, and immunologists will likely be essential. Solutions to most of the profound problems for which high-Q devices are well-suited will ultimately involve highly collaborative interactions between multiple, seemingly disparate scientific areas.

Though many of the challenges outlined above are significant, the field of high-Q optical sensors is young, vibrant, and continuously expanding. Keeping in mind that great strides in assay design and surface chemistry have been made in just the last few years, it is clear that

the field has not reached maturity. The next few years should witness continued progress in enhancement of assay sensitivity and specificity, integration into user-friendly lab-on-a-chip formats, and application to previously intractable problems. Stimulating collaborations should develop naturally as the impressive capabilities of these sensors become more widely known. These collaborations should help to shift the field's focus from that of optimizing Q factors and detecting model proteins to that of creating robust assays for defined targets in systems where traditional tools are insufficient. Although a great deal of interdisciplinary progress must be made to realize the lofty goal of ultrasensitive, multiplexed, and real-time chemical and biomolecular detection, the future for high-Q optical sensors will likely include exciting advancements with previously intractable analytical challenges.

Biographies

Matthew S. Luchansky is a National Science Foundation Graduate Research Fellow and Ph.D. candidate in the Department of Chemistry at the University of Illinois at Urbana-Champaign. He received a B.S. in Chemistry and a B.A. in Economics from the University of Richmond in 2008. At Richmond, he performed biochemical and structural characterization of a novel thermophilic protein under the direction of Jonathan Dattelbaum. His research in the lab of Ryan Bailey focuses on the development of silicon photonic microring resonator technology for multiplexed protein biosensing, with applications in T cell cytokine secretion profiling, serum biomarker analysis, and in vitro diagnostics.

Ryan C. Bailey received his B.S. in Chemistry from Eastern Illinois University in 1999 and continued his studies at Northwestern University, where he obtained his Ph.D. in Chemistry in 2004 under the direction of Joseph Hupp. Following a joint post-doctoral fellowship at the California Institute of Technology and the Institute for Systems Biology with James Heath and Leroy Hood, respectively, Ryan joined the faculty in the Department of Chemistry at the University of Illinois at Urbana-Champaign in 2006. He is also affiliated with the University's Department of Bioengineering, Micro and Nanotechnology Laboratory, and Institute for Genomic Biology. His lab focuses on developing innovative analytical and biomaterials solutions for a range of challenges at the interface of chemistry and biology, with particular interests in silicon photonics, as well as functional and responsive biomaterials. In recognition of his accomplishments, he has been recognized with a New Faculty Award from the Camille and Henry Dreyfus Foundation, a Director's New Innovator Award from the National Institutes of Health, and was named a fellow of the Alfred P. Sloan Foundation.

Acknowledgments

In support of our own efforts to develop high Q-factor optical microcavities, we acknowledge the NIH Director's New Innovator Award Program, part of the NIH Roadmap for Medical Research, through grant number 1-DP2-OD002190-01, and from the Camille and Henry Dreyfus Foundation. M.S.L is supported by a National Science Foundation Graduate Research Fellowship and a Robert C. and Carolyn J. Springborn Fellowship from the University of Illinois at Urbana-Champaign. R.C.B. is a research fellow of the Alfred P. Sloan Foundation.

References

1. It is worth noting that label-free sensors often involve a specific capture agent such as an antibody, complementary DNA probe, or aptamer that causes the detection methodology to be no longer rigorously label-free. However, the biosensing community has firmly established the designation of "label-free" to include sensors that may require specific recognition elements but do not require fluorescent or enzymatic tags, and that broader definition of "label-free" will be used in this review.
2. Vollmer F, Arnold S. Nat. Methods. 2008; 5:591–596. [PubMed: 18587317]

3. Luchansky MS, Washburn AL, Martin TA, Iqbal M, Gunn LC, Bailey RC. Biosens. Bioelectron. 2010; 26:1283–1291. [PubMed: 20708399]
4. Cunningham BT. JALA. 2010; 15:120–135. [PubMed: 20383277]
5. Qavi AJ, Washburn AL, Byeon J-Y, Bailey RC. Anal. Bioanal. Chem. 2009; 394:121–135. [PubMed: 19221722]
6. Goddard, J.; Mandal, S.; Erickson, D. Advanced photonic structures for biological and chemical detection. Fan, X., editor. Vol. Vol. III. New York: Springer; 2009. p. 445-470.
7. Fan X, White IM, Shopova SI, Zhu H, Suter JD, Sun Y. Anal. Chim. Acta. 2008; 620:8–26. [PubMed: 18558119]
8. Hunt HK, Armani AM. Nanoscale. 2010; 2:1544–1559. [PubMed: 20820687]
9. Feng S, Lei T, Chen H, Cai H, Luo X, Poon AW. Laser Photonics Rev. 2011 *in press*.
10. Passaro VMN, Dell'Olio F, Casamassima B, De Leonardis F. Sensors. 2007; 7:508–536.
11. Washburn AL, Bailey RC. Analyst. 2011; 136:227–236. [PubMed: 20957245]
12. Donzella V, Crea F. J. Biophotonics. 2011; 4:442–452. [PubMed: 21567973]
13. Estevez MC, Alvarez M, Lechuga LM. Laser Photonics Rev. 2011 *in press*.
14. Sohlström H, Gylfason KB, Hill D. Proc. SPIE. 2010; 7719:77190B 1–77190B 15.
15. Sun Y, Fan X. Anal. Bioanal. Chem. 2011; 399:205–211. [PubMed: 20938769]
16. Ward J, Benson O. Laser Photonics Rev. 2011; 5:553–570.
17. Shamah SM, Cunningham BT. Analyst. 2011; 136:1090–1102. [PubMed: 21279202]
18. Jokerst N, Royal M, Palit S, Luan L, Dhar S, Tyler T. J. Biophotonics. 2009; 2:212–226. [PubMed: 19367589]
19. Monat C, Domachuk P, Eggleton BJ. Nature Photon. 2007; 1:106–114.
20. Arlett JL, Myers EB, Roukes ML. Nature Nanotech. 2011; 6:203–215.
21. Yoshie T, Tang L, Su S-Y. Sensors. 2011; 11:1972–1991.
22. Weiss SM, Rong G, Lawrie JL. Physica E. 2009; 41:1071–1075.
23. Strutt JW. Philos. Mag. 1910; 20:1001–1004.
24. Li H, Fan X. Appl. Phys. Lett. 2010; 97:011105 1–011105 3.
25. Arnold S, Khoshsima M, Teraoka I, Holler S, Vollmer F. Opt. Lett. 2003; 28:272–274. [PubMed: 12653369]
26. Reed, GT.; Knights, AP. Silicon photonics. West Sussex, England: John Wiley and Sons, Ltd; 2004.
27. Min B, Ostby E, Sorger V, Ulin-Avila E, Yang L, Zhang X, Vahala K. Nature. 2009; 457:455–458. [PubMed: 19158793]
28. Zhang X, Choi HS, Armani AM. Appl. Phys. Lett. 2010; 96:153304 1–153304 3.
29. Armani DK, Kippenberg TJ, Spillane SM, Vahala KJ. Nature. 2003; 421:925–928. [PubMed: 12606995]
30. Armani, A.; Chremmos, I.; Schwelb, O.; Uzunoglu, N. Photonic microresonator research and applications. Chremmos, I.; Schwelb, O.; Uzunoglu, N., editors. Vol. Vol. 156. Berlin: Springer; 2010. p. 253-273.
31. Marcatili EAJ. Bell Labs Technical Journal. 1969; 48:2071–2102.
32. Little BE, Foresi JS, Steinmeyer G, Thoen ER, Chu ST, Haus HA, Ippen EP, Kimerling LC, Greene W. IEEE Photon. Technol. Lett. 1998; 10:549–551.
33. Madsen CK, Lenz G. IEEE Photon. Technol. Lett. 1998; 10:994–996.
34. Little BE, Chu ST, Haus HA, Foresi J, Laine J-P. J. Lightwave Technol. 1997; 15:998–1005.
35. Serpengüzel A, Arnold S, Griffel G. Opt. Lett. 1995; 20:654–656. [PubMed: 19859286]
36. Boyd RW, Heebner JE. Appl. Opt. 2001; 40:5742–5747. [PubMed: 18364865]
37. Cai M, Painter O, Vahala KJ. Phys. Rev. Lett. 2000; 85:74–77. [PubMed: 10991162]
38. Little BE, Chu ST. Opt. Photon. News. 2000; 11:24–29.
39. Vollmer F, Braun D, Libchaber A, Khoshsima M, Teraoka I, Arnold S. Appl. Phys. Lett. 2002; 80:4057–4059.

40. Yalcin A, Popat KC, Aldridge JC, Desai TA, Hryniewicz J, Chbouki N, Little BE, King O, Van V, Chu S, Gill D, Anthes-Washburn M, Unlu MS, Goldberg BB. IEEE J. Sel. Top. Quantum Electron. 2006; 12:148–155.
41. Zhu H, White IM, Suter JD, Dale PS, Fan X. Opt. Express. 2007; 15:9139–9146. [PubMed: 19547254]
42. Armani AM, Kulkarni RP, Fraser SE, Flagan RC, Vahala KJ. Science. 2007; 317:783–787. [PubMed: 17615303]
43. Iqbal M, Gleeson MA, Spaugh B, Tybor F, Gunn WG, Hochberg M, Baehr-Jones T, Bailey RC, Gunn LC. IEEE J. Sel. Top. Quantum Electron. 2010; 16:654–661.
44. Gylfason KB, Carlborg CF, Kazmierczak A, Dortu F, Sohlström H, Vivien L, Barrios CA, van der Wijngaart W, Stemme G. Opt. Express. 2010; 18:3226–3237. [PubMed: 20389330]
45. Washburn AL, Luchansky MS, Bowman AL, Bailey RC. Anal. Chem. 2010; 82:69–72. [PubMed: 20000326]
46. Mandal S, Goddard JM, Erickson D. Lab Chip. 2009; 9:2924–2932. [PubMed: 19789745]
47. Xu DX, Vachon M, Densmore A, Ma R, Delâge A, Janz S, Lapointe J, Li Y, Lopinski G, Zhang D, Liu QY, Cheben P, Schmid JH. Opt. Lett. 2010; 35:2771–2773. [PubMed: 20717452]
48. Ling T, Guo LJ. J. Opt. Soc. Am. B. 2009; 26:471–477.
49. Watts MR. Opt. Lett. 2010; 35:3231–3233. [PubMed: 20890343]
50. Sonnefraud Y, Verellen N, Sobhani H, Vandenbosch GAE, Moshchalkov VV, Van Dorpe P, Nordlander P, Maier SA. ACS Nano. 2010; 4:1664–1670. [PubMed: 20155967]
51. Claes T, Bogaerts W, Bienstman P. Opt. Express. 2010; 18:22747–22761. [PubMed: 21164613]
52. Roy S, Prasad M, Topolancik J, Vollmer F. J. Appl. Phys. 2010; 107:053115 1–053115 9.
53. Santiago-Cordoba MA, Boriskina SV, Vollmer F, Demirel MC. Appl. Phys. Lett. 2011; 99:073701 1–073701 3.
54. Ren HC, Vollmer F, Arnold S, Libchaber A. Opt. Express. 2007; 15:17410–17423. [PubMed: 19551035]
55. Saetchnikov V, Tcherniavskaia E. J. Appl. Spectrosc. 2010; 77:714–721.
56. Vollmer F, Arnold S, Keng D. Proc. Natl. Acad. Sci. U. S. A. 2008; 105:20701–20704. [PubMed: 19075225]
57. Vollmer F, Arnold S. Proc. SPIE. 2009; 7397:739702 1–739702 9.
58. Tcherniavskaia E, Saetchnikov V. J. Appl. Spectrosc. 2010; 77:692–699.
59. Lin N, Jiang L, Wang S, Xiao H, Lu Y, Tsai H. Appl. Opt. 2011; 50:992–998. [PubMed: 21364722]
60. Lin N, Jiang L, Wang S, Yuan L, Xiao H, Lu Y, Tsai H. Appl. Opt. 2010; 49:6463–6471. [PubMed: 21102672]
61. Charlebois M, Paquet A, Verret L, Boissinot K, Boissinot M, Bergeron M, Allen C. Nanoscale Res. Lett. 2010; 5:524–532. [PubMed: 20672075]
62. Himmelhaus M, Krishnamoorthy S, Francois A. Sensors. 2010; 10:6257–6274. [PubMed: 22219711]
63. Beier H, Cote G, Meissner K. Ann. Biomed. Eng. 2009; 37:1974–1983. [PubMed: 19462236]
64. Chew H. J. Chem. Phys. 1987; 87:1355–1360.
65. Hunt HK, Armani AM. Opt. Lett. 2011; 36:1092–1094. [PubMed: 21478993]
66. Armani AM, Srinivasan A, Vahala KJ. Nano Lett. 2007; 7:1823–1826. [PubMed: 17516682]
67. Choi HS, Zhang X, Armani AM. Opt. Lett. 2010; 35:459–461. [PubMed: 20160783]
68. Xiao Y-F, Zou C-L, Li B-B, Li Y, Dong C-H, Han Z-F, Gong Q. Phys. Rev. Lett. 2010; 105:153902 1–153902 4. [PubMed: 21230906]
69. Krioukov E, Klunder DJW, Driessen A, Greve J, Otto C. Opt. Lett. 2002; 27:512–514. [PubMed: 18007849]
70. Kippenberg TJ, Kalkman J, Polman A, Vahala KJ. Phys. Rev. A. 2006; 74 051802.
71. Lee S, Eom SC, Chang JS, Huh C, Sung GY, Shin JH. Opt. Express. 2010; 18:11209–11215. [PubMed: 20588980]

72. Lee S, Eom SC, Chang JS, Huh C, Sung GY, Shin JH. Opt. Express. 2010; 18:20638–20644. [PubMed: 20940958]
73. Hu J, Carlie N, Feng N-N, Petit L, Agarwal A, Richardson K, Kimerling L. Opt. Lett. 2008; 33:2500–2502. [PubMed: 18978900]
74. Grossmann T, Hauser M, Beck T, Gohn-Kreuz C, Karl M, Kalt H, Vannahme C, Mappes T. Appl. Phys. Lett. 2010; 96:013303 1–013303 3.
75. Chen Y-H, Guo L. Plasmonics. 2011; 6:183–188.
76. Ramachandran A, Wang S, Clarke J, Ja SJ, Goad D, Wald L, Flood EM, Knobbe E, Hryniewicz JV, Chu ST, Gill D, Chen W, King O, Little BE. Biosens. Bioelectron. 2008; 23:939–944. [PubMed: 17964774]
77. Barrios CA, Gylfason KB, Sánchez B, Griol A, Sohlström H, Holgado M, Casquel R. Opt. Lett. 2007; 32:3080–3082. [PubMed: 17975603]
78. Barrios CA, Bañuls MJ, González-Pedro V, Gylfason KB, Sánchez B, Griol A, Maquieira A, Sohlström H, Holgado M, Casquel R. Opt. Lett. 2008; 33:708–710. [PubMed: 18382525]
79. Xu DX, Densmore A, Delâge A, Waldron P, McKinnon R, Janz S, Lapointe J, Lopinski G, Mischki T, Post E, Cheben P, Schmid JH. Opt. Express. 2008; 16:15137–15148. [PubMed: 18795053]
80. De Vos K, Bartolozzi I, Schacht E, Bienstman P, Baets R. Opt. Express. 2007; 15:7610–7615. [PubMed: 19547087]
81. Bailey RC, Washburn AL, Qavi AJ, Iqbal M, Gleeson M, Tybor F, Gunn LC. Proc. SPIE. 2009; 7220:1–6. 72200N.
82. Chao CY, Fung W, Guo LJ. IEEE J. Sel. Top. Quantum Electron. 2006; 12:134–142.
83. Ling T, Chen SL, Guo LJ. Appl. Phys. Lett. 2011; 98:1–3. 204103.
84. Kim GD, Son GS, Lee HS, Kim KD, Lee SS. Opt. Commun. 2008; 281:4644–4647.
85. Zhou L, Sun X, Li X, Chen J. Sensors. 2011; 11:6856–6867. [PubMed: 22163989]
86. Wiley BJ, Qin D, Xia Y. ACS Nano. 2010; 4:3554–3559. [PubMed: 20695512]
87. Washburn AL, Gunn LC, Bailey RC. Anal. Chem. 2009; 81:9499–9506. [PubMed: 19848413]
88. Sun R, Cheng J, Michel J, Kimerling L. Opt. Lett. 2009; 34:2378–2380. [PubMed: 19649103]
89. Chao CY, Guo LJ. Appl. Phys. Lett. 2003; 83:1527–1529.
90. Ling T, Chen SL, Guo LJ. Opt. Express. 2011; 19:861–869. [PubMed: 21263625]
91. Oulton RF, Sorger VJ, Genov DA, Pile DFP, Zhang X. Nature Photon. 2008; 2:496–500.
92. Mancinelli M, Guider R, Bettotti P, Masi M, Vanacharla MR, Fedeli JM, Thourhout DV, Pavesi L. J. Nanophoton. 2011; 5:1–8. 051705.
93. Flueckiger J, Grist SM, Bisra G, Chrostowski L, Cheung KC. Proc. SPIE. 2011; 7929:1–10. 79290I.
94. Li X, Zhang Z, Qin S, Wang T, Liu F, Qiu M, Su Y. Appl. Opt. 2009; 48:F90–F94. [PubMed: 19724320]
95. Densmore A, Vachon M, Xu DX, Janz S, Ma R, Li YH, Lopinski G, Delage A, Lapointe J, Luebbert CC, Liu QY, Cheben P, Schmid JH. Opt. Lett. 2009; 34:3598–3600. [PubMed: 19953132]
96. Wang S, Broderick K, Smith H, Yi Y. Appl. Phys. Lett. 2010; 97:1–3. 051102.
97. De Vos K, Girones J, Claes T, De Koninck Y, Popelka S, Schacht E, Baets R, Bienstman P. IEEE Photon. J. 2009; 1:225–235.
98. Carlborg CF, Gylfason KB, Kazmierczak A, Dortu F, Polo MJB, Catala AM, Kresbach GM, Sohlstrom H, Moh T, Vivien L, Popplewell J, Ronan G, Barrios CA, Stemme G, van derWijngaart W. Lab Chip. 2010; 10:281–290. [PubMed: 20090999]
99. White IM, Oveys H, Fan X. Opt. Lett. 2006; 31:1319–1321. [PubMed: 16642098]
100. White, IM.; Zhu, H.; Suter, JD.; Fan, X.; Zourob, M. Methods in molecular biology : Biosensors and biodetection. Rasooly, A.; Herold, KE., editors. Vol. Vol. 503. New York, NY: Humana Press; 2009. p. 139-165.
101. Zamora V, Díez A, Andrés MV, Gimeno B. Proc. SPIE. 2009; 7356:1–8. 73560Z.

102. Lin N, Jiang L, Wang S, Xiao H, Lu Y, Tsai HL. Appl. Opt. 2011; 50:3615–3621. [PubMed: 21743574]
103. Zhu H, White IM, Suter JD, Zourob M, Fan X. Anal. Chem. 2007; 79:930–937. [PubMed: 17263318]
104. Bernardi A, Kiravittaya S, Rastelli A, Songmuang R, Thurmer DJ, Benyoucef M, Schmidt OG. Appl. Phys. Lett. 2008; 93:1–3. 094106.
105. Zamora V, Díez A, Andrés MV, Gimeno B. Opt. Express. 2007; 15:12011–12016. [PubMed: 19547565]
106. Shopova SI, White IM, Sun Y, Zhu H, Fan X, Frye-Mason G, Thompson A, Ja Sj. Anal. Chem. 2008; 80:2232–2238. [PubMed: 18271605]
107. Liu J, Sun Y, Howard DJ, Frye-Mason G, Thompson AK, Ja Sj, Wang SK, Bai M, Taub H, Almasri M, Fan X. Anal. Chem. 2010; 82:4370–4375. [PubMed: 20441156]
108. Sun Y, Liu J, Howard DJ, Frye-Mason G, Thompson AK, Ja Sj, Fan X. Analyst. 2010; 135:165–171. [PubMed: 20024197]
109. Koch B, Carson L, Guo CM, Lee CY, Yi Y, Zhang JY, Zin M, Znameroski S, Smith T. Sens. Actuators, B. 2010; 147:573–580.
110. Sumetsky M, Dulashko Y, Windeler RS. Opt. Lett. 2010; 35:898–900. [PubMed: 20364162]
111. Claes T, Molera JG, De Vos K, Schacht E, Baets R, Bienstman P. IEEE Photon. J. 2009; 1:197–204.
112. Koch B, Yi Y, Zhang JY, Znameroski S, Smith T. Appl. Phys. Lett. 2009; 95:1–3. 201111.
113. Almeida VR, Xu Q, Barrios CA, Lipson M. Opt. Lett. 2004; 29:1209–1211. [PubMed: 15209249]
114. Kargar A, Chao CY. J. Opt. Soc. Am. A. 2011; 28:596–603.
115. Guo Y, Ye JY, Divin C, Huang B, Thomas TP, Baker JJR, Norris TB. Anal. Chem. 2010; 82:5211–5218. [PubMed: 20486666]
116. Yang D, Tian H, Ji Y. Opt. Eng. 2011; 50:1–6. 054402.
117. Kim MK, Kim JY, Kang JH, Ahn BH, Lee YH. Laser Photonics Rev. 2011; 5:479–495.
118. Kuramochi E, Taniyama H, Tanabe T, Kawasaki K, Roh YG, Notomi M. Opt. Express. 2010; 18:15859–15869. [PubMed: 20720968]
119. Tang L, Yoshie T. Opt. Express. 2007; 15:17254–17263. [PubMed: 19551019]
120. Nair RV, Vijaya R. Prog. Quant. Electron. 2010; 34:89–134.
121. Choi CJ, Cunningham BT. Lab Chip. 2007; 7:550–556. [PubMed: 17476372]
122. Song BS, Noda S, Asano T, Akahane Y. Nature Mater. 2005; 4:207–210.
123. Dorfner D, Zabel T, Hurlimann T, Hauke N, Frandsen L, Rant U, Abstreiter G, Finley J. Biosens. Bioelectron. 2009; 24:3688–3692. [PubMed: 19501502]
124. Zlatanovic S, Mirkarimi LW, Sigalas MM, Bynum MA, Chow E, Robotti KM, Burr GW, Esener S, Grot A. Sens. Actuators, B. 2009; 141:13–19.
125. Ganesh N, Zhang W, Mathias PC, Chow E, Soares JANT, Malyarchuk V, Smith AD, Cunningham BT. Nature Nanotech. 2007; 2:515–520.
126. Ishizaki K, Noda S. Nature. 2009; 460:367–370. [PubMed: 19606144]
127. George S, Block ID, Jones SI, Mathias PC, Chaudhery V, Vuttipittayamongkol P, Wu HY, Vodkin LO, Cunningham BT. Anal. Chem. 2010; 82:8551–8557. [PubMed: 20857905]
128. Huang CS, George S, Lu M, Chaudhery V, Tan R, Zangar RC, Cunningham BT. Anal. Chem. 2011; 83:1425–1430. [PubMed: 21250635]
129. Kang C, Phare CT, Vlasov YA, Assefa S, Weiss SM. Opt. Express. 2010; 18:27930–27937. [PubMed: 21197066]
130. Sunner T, Stichel T, Kwon SH, Schlereth TW, Hofling S, Kamp M, Forchel A. Appl. Phys. Lett. 2008; 92:1–3. 261112.
131. Yu X, Shi L, Han D, Zi J, Braun PV. Adv. Funct. Mater. 2010; 20:1910–1916.
132. Mathias PC, Ganesh N, Cunningham BT. Anal. Chem. 2008; 80:9013–9020. [PubMed: 19551930]
133. Vollmer F, Arnold S, Braun D, Teraoka I, Libchaber A. Biophys. J. 2003; 85:1974. [PubMed: 12944310]

134. Densmore A, Xu DX, Janz S, Waldron P, Mischki T, Lopinski G, Delage A, Lapointe J, Cheben P, Lamontagne B, Schmid JH. Opt. Lett. 2008; 33:596–598. [PubMed: 18347721]
135. Qavi AJ, Bailey RC. Angew. Chem. Int. Ed. 2010; 49:4608–4611.
136. Hunt HK, Soteropulos C, Armani AM. Sensors. 2010; 10:9317–9336. [PubMed: 22163409]
137. Qavi AJ, Kindt JT, Gleeson MA, Bailey RC. Anal. Chem. 2011; 83:5949–5956. [PubMed: 21711056]
138. Zhu HY, White IM, Suter JD, Fan XD. Biosens. Bioelectron. 2008; 24:461–466. [PubMed: 18550355]
139. Zhu H, Dale PS, Caldwell CW, Fan X. Anal. Chem. 2009; 81:9858–9865. [PubMed: 19911811]
140. Byeon JY, Limpoco FT, Bailey RC. Langmuir. 2010; 26:15430–15435. [PubMed: 20809595]
141. Hermanson, GT. Bioconjugate techniques. San Diego, CA: Academic Press; 1996.
142. Suter JD, White IM, Zhu H, Shi H, Caldwell CW, Fan X. Biosens. Bioelectron. 2008; 23:1003–1009. [PubMed: 18036809]
143. Gohring JT, Dale PS, Fan X. Sens. Actuators, B. 2010; 146:226–230.
144. Qavi AJ, Mysz TM, Bailey RC. Anal. Chem. 2011; 83:6827–6833. [PubMed: 21834517]
145. Luchansky MS, Bailey RC. Anal. Chem. 2010; 82:1975–1981. [PubMed: 20143780]
146. Fukuyama M, Yamatogi S, Ding H, Nishida M, Kawamoto C, Amemiya Y, Ikeda T, Noda T, Kawamoto S, Ono K, Kuroda A, Yokoyama S. Jpn. J. Appl. Phys. 2010; 49:1–4. 04DL09.
147. Landgraf R, Kaiser MK, Posseckardt J, Adolphi B, Fischer WJ. Procedia Chemistry. 2009; 1:1015–1018.
148. Heeres JT, Kim SH, Leslie BJ, Lidstone EA, Cunningham BT, Hergenrother PJ. J. Am. Chem. Soc. 2009; 131:18202–18203. [PubMed: 19968284]
149. Benters R, Niemeyer CM, Drutschmann D, Blohm D, Wohrle D. Nucleic Acids Res. 2002; 30:1–7. e10. [PubMed: 11752241]
150. Ikeda T, Hata Y, Ninomiya Ki, Ikura Y, Takeguchi K, Aoyagi S, Hirota R, Kuroda A. Anal. Biochem. 2009; 385:132–137. [PubMed: 19017523]
151. Sun Y, Liu J, Frye-Mason G, Ja Sj, Thompson AK, Fan X. Analyst. 2009; 134:1386–1391. [PubMed: 19562206]
152. Orghici R, Lutzow P, Burgmeier J, Koch J, Heidrich H, Schade W, Welschoff N, Waldvogel S. Sensors. 2010; 10:6788–6795. [PubMed: 22163576]
153. Lubczyk D, Siering C, Lorgen J, Shifrina ZB, Mullen K, Waldvogel SR. Sens. Actuators, B. 2010; 143:561–566.
154. Yebo NA, Lommens P, Hens Z, Baets R. Opt. Express. 2010; 18:11859–11866. [PubMed: 20589047]
155. Yebo NA, Taillaert D, Roels J, Lahem D, Debliquy M, Van Thourhout D, Baets R. IEEE Photon. Technol. Lett. 2009; 21:960–962.
156. Byeon JY, Bailey RC. Analyst. 2011; 136:3430–3433. [PubMed: 21085731]
157. Luchansky MS, Bailey RC. J. Am. Chem. Soc. 2011 *in press*.
158. Kirk JT, Fridley GE, Chamberlain JW, Christensen ED, Hochberg M, Ratner DM. Lab Chip. 2011; 11:1372–1377. [PubMed: 21327248]
159. Washburn AL, Gomez J, Bailey RC. Anal. Chem. 2011; 83:3572–3580. [PubMed: 21438633]
160. Xu DX, Vachon M, Densmore A, Ma R, Janz S, Delâge A, Lapointe J, Cheben P, Schmid JH, Post E, Messaoudène S, Fédéli JM. Opt. Express. 2010; 18:22867–22879. [PubMed: 21164626]
161. Bailey RC, Kwong GA, Radu CG, Witte ON, Heath JR. J. Am. Chem. Soc. 2007; 129:1959–1967. [PubMed: 17260987]
162. Unsworth LD, Sheardown H, Brash JL. Langmuir. 2008; 24:1924–1929. [PubMed: 18217777]
163. Jiang S, Cao Z. Adv. Mater. 2010; 22:920–932. [PubMed: 20217815]
164. De Vos K, Girones J, Popelka S, Schacht E, Baets R, Bienstman P. Biosens. Bioelectron. 2009; 24:2528–2533. [PubMed: 19200711]
165. Limpoco FT, Bailey RC. J. Am. Chem. Soc. 2011; 133:14864–14867. [PubMed: 21899288]
166. Zhu H, White IM, Suter JD, Zourob M, Fan X. Analyst. 2008; 133:356–360. [PubMed: 18299750]

167. Ye WN, Michel J, Kimerling LC. IEEE Photon. Technol. Lett. 2008; 20:885–887.
168. Suter JD, White IM, Zhu H, Fan X. Appl. Opt. 2007; 46:389–396. [PubMed: 17228386]
169. Huckabay HA, Dunn RC. Sens. Actuators, B. 2011 *in press*.
170. Wang S, Ramachandran A, Ja S-J. Biosens. Bioelectron. 2009; 24:3061–3066. [PubMed: 19380222]
171. Squires TM, Messinger RJ, Manalis SR. Nat. Biotechnol. 2008; 26:417–426. [PubMed: 18392027]
172. Sheehan PE, Whitman LJ. Nano Lett. 2005; 5:803–807. [PubMed: 15826132]
173. Choi CJ, Belobraydich AR, Chan LL, Mathias PC, Cunningham BT. Anal. Biochem. 2010; 405:1–10. [PubMed: 20553867]
174. Abdelgawad M, Wheeler AR. Adv. Mater. 2009; 21:920–925.
175. Luan L, Evans RD, Jokerst NM, Fair RB. IEEE Sens. J. 2008; 8:628–635.
176. Lu T, Lee H, Chen T, Herchak S, Kim J-H, Fraser SE, Flagan RC, Vahala K. Proc. Natl. Acad. Sci. U. S. A. 2011; 108:5976–5979. [PubMed: 21444782]
177. Luchansky MS, Washburn AL, McClellan MS, Bailey RC. Lab Chip. 2011; 11:2042–2044. [PubMed: 21541438]
178. Witzens J, Hochberg M. Opt. Express. 2011; 19:7034–7061. [PubMed: 21503017]
179. Cheng W, Yan F, Ding L, Ju H, Yin Y. Anal. Chem. 2010; 82:3337–3342. [PubMed: 20345087]
180. Konry T, Hayman RB, Walt DR. Anal. Chem. 2009; 81:5777–5782. [PubMed: 19548682]
181. Li Y, Lee HJ, Corn RM. Anal. Chem. 2007; 79:1082–1088. [PubMed: 17263339]
182. Fang S, Lee HJ, Wark AW, Corn RM. J. Am. Chem. Soc. 2006; 128:14044–14046. [PubMed: 17061884]
183. Kim S, Lee J, Lee SJ, Lee HJ. Talanta. 2010; 81:1755–1759. [PubMed: 20441969]
184. Sim HR, Wark AW, Lee HJ. Analyst. 2010; 135:2528–2532. [PubMed: 20725693]
185. Choi J, Routenberg Love K, Gong Y, Gierahn TM, Love JC. Anal. Chem. 2011; 83:6890–6895. [PubMed: 21812465]
186. Blair S, Chen Y. Appl. Opt. 2001; 40:570–582. [PubMed: 18357033]
187. García-Rupérez J, Toccafondo V, Bañuls MJ, Castelló JG, Griol A, Peransi-Llopis S, Maquieira Á. Opt. Express. 2010; 18:24276–24286. [PubMed: 21164773]
188. Suter JD, Howard DJ, Shi H, Caldwell CW, Fan X. Biosens. Bioelectron. 2010; 26:1016–1020. [PubMed: 20846848]
189. Chan LL, Pineda M, Heeres JT, Hergenrother PJ, Cunningham BT. ACS Chem. Biol. 2008; 3(437):448.
190. Arnold S, Shopova SI, Holler S. Opt. Express. 2010; 18:281–287. [PubMed: 20173848]
191. Haddad JJ. Biochem. Biophys. Res. Commun. 2002; 297:700–713. [PubMed: 12359210]
192. Anderson NL, Anderson NG. Mol. Cell Proteomics. 2002; 1:845–867. [PubMed: 12488461]
193. Gohring JT, Fan X. Sensors. 2010; 10:5798–5808. [PubMed: 22219687]
194. McClellan MS, Bailey RC. Biosens. Bioelectron. 2011 *in press*.
195. Wilson KA, Finch CA, Anderson P, Vollmer F, Hickman JJ. Biomaterials. 2011 *in press*.
196. Freeman LM, Li S, Dayani Y, Choi H-S, Malmstadt N, Armani AM. Appl. Phys. Lett. 2011; 98:1–3. 143703.
197. Block ID, Mathias PC, Ganesh N, Jones SI, Dorvel BR, Chaudhery V, Vodkin LO, Bashir R, Cunningham BT. Opt. Express. 2009; 17:13222–13235. [PubMed: 19654728]
198. Lidstone EA, Chaudhery V, Kohl A, Chan V, Wolf-Jensen T, Schook LB, Bashir R, Cunningham BT. Analyst. 2011; 136:3608–3615. [PubMed: 21691654]
199. Robinson JT, Chen L, Lipson M. Opt. Express. 2008; 16:4296–4301. [PubMed: 18542525]
200. Gregor M, Pyrlik C, Henze R, Wicht A, Peters A, Benson O. Appl. Phys. Lett. 2010; 96:1–3. 231102.
201. Choi HS, Ismail S, Armani AM. Opt. Lett. 2011; 36:2152–2154. [PubMed: 21633479]
202. Vollmer F, Fischer P. Opt. Lett. 2006; 31:453–455. [PubMed: 16496884]
203. Topolancik J, Vollmer F. Biophys. J. 2007; 92:2223–2229. [PubMed: 17208972]

204. Noto M, Keng D, Teraoka I, Arnold S. Biophys. J. 2007; 92:4466–4472. [PubMed: 17400701]
205. Nitkowski A, Baeumner A, Lipson M. Biomed. Opt. Express. 2011; 2:271–277. [PubMed: 21339873]
206. Tan Y, Ge C, Chu A, Lu M, Goldshlag W, Huang C, Pokhriyal A, George S, Cunningham B. IEEE Sens. J. 2011 *in press*.
207. Li H, Guo Y, Sun Y, Reddy K, Fan X. Opt. Express. 2010; 18:25081–25088. [PubMed: 21164854]
208. Lagos N, Sigalas MM. Sens. Actuators, B. 2011; 153:252–255.
209. Haddadpour A, Yi Y. Biomed. Opt. Express. 2010; 1:378–384. [PubMed: 21258474]
210. Zhu J, Ozdemir SK, Xiao Y-F, Li L, He L, Chen D-R, Yang L. Nature Photon. 2010; 4:46–49.
211. Keng D, McAnanama SR, Teraoka I, Arnold S. Appl. Phys. Lett. 2007; 91:1–3. 103902.
212. Yang AHJ, Erickson D. Lab Chip. 2010; 10:769–774. [PubMed: 20221566]
213. Cai H, Poon AW. Opt. Lett. 2010; 35:2855–2857. [PubMed: 20808347]
214. Lin S, Schonbrun E, Crozier K. Nano Lett. 2010; 10:2408–2411. [PubMed: 20545333]
215. Mandal S, Serey X, Erickson D. Nano Lett. 2010; 10:99–104. [PubMed: 19957918]
216. Arnold S, Keng D, Shopova SI, Holler S, Zurawsky W, Vollmer F. Opt. Express. 2009; 17:6230–6238. [PubMed: 19365447]
217. Serey X, Mandal S, Erickson D. Nanotechnology. 2010; 21:1–8. 305202.
218. Liang D, Fiorentino M, Okumura T, Chang H-H, Spencer DT, Kuo Y-H, Fang AW, Dai D, Beausoleil RG, Bowers JE. Opt. Express. 2009; 17:20355–20364. [PubMed: 19997264]
219. Wang QJ, Yan C, Yu N, Unterhinninghofen J, Wiersig J, Pflugl C, Diehl L, Edamura T, Yamanishi M, Kan H, Capasso F. Proc. Natl. Acad. Sci. U. S. A. 2010; 107:22407–22412. [PubMed: 21149678]
220. Li H, Shang L, Tu X, Liu L, Xu L. J. Am. Chem. Soc. 2009; 131:16612–16613. [PubMed: 19919131]
221. Shang L, Liu L, Xu L. Opt. Lett. 2008; 33:1150–1152. [PubMed: 18483542]
222. Lee W, Li H, Suter JD, Reddy K, Sun Y, Fan X. Appl. Phys. Lett. 2011; 98:1–3. 061103.
223. Sun Y, Suter JD, Fan X. Opt. Lett. 2009; 34:1042–1044. [PubMed: 19340213]
224. Sun Y, Shopova SI, Wu C-S, Arnold S, Fan X. Proc. Natl. Acad. Sci. U. S. A. 2010; 107:16039–16042. [PubMed: 20798062]
225. Yang J-K, Noh H, Rooks MJ, Solomon GS, Vollmer F, Cao H. Appl. Phys. Lett. 2011; 98:1–3. 241107.
226. Kita S, Hachuda S, Nozaki K, Baba T. Appl. Phys. Lett. 2010; 97:1–3. 161108.
227. Liang D, Bowers JE. Nature Photon. 2010; 4:511–517.
228. Kim G-D, Lee H-S, Park C-H, Lee S-S, Lim BT, Bae HK, Lee W-G. Opt. Express. 2010; 18:22215–22221. [PubMed: 20941123]
229. Li B-B, Wang Q-Y, Xiao Y-F, Jiang X-F, Li Y, Xiao L, Gong Q. Appl. Phys. Lett. 2010; 96:1–3. 251109.
230. Watts MR, Shaw MJ, Nielson GN. Nature Photon. 2007; 1:632–634.
231. Rosenberg J, Shenoi RV, Krishna S, Painter O. Opt. Express. 2010; 18:3672–3686. [PubMed: 20389377]
232. Boriskina SV, Reinhard BM. Proc. Natl. Acad. Sci. U. S. A. 2011; 108:3147–3151. [PubMed: 21300898]
233. Dai D, He S. J. Opt. Soc. Am. B. 2009; 26:511–516.
234. Terrel M, Digonnet MJF, Fan S. Appl. Opt. 2009; 48:4874–4879. [PubMed: 19745847]
235. Yi H, Citrin DS, Chen Y, Zhou Z. Appl. Phys. Lett. 2009; 95:1–3. 191112.
236. Kang Y, Arbabi A, Goddard L. Opt. Quant. Electron. 2009; 41:689–697.
237. Arbabi A, Kang YM, Lu C-Y, Chow E, Goddard LL. Appl. Phys. Lett. 2011; 99:1–3. 091105.
238. Kang YM, Arbabi A, Goddard LL. Opt. Express. 2010; 18:16813–16825. [PubMed: 20721073]
239. Kodadek T, Reddy MM, Olivos HJ, Bachhawat-Sikder K, Alluri PG. Acc. Chem. Res. 2004; 37:711–718. [PubMed: 15379586]

240. Sefah K, Phillips JA, Xiong X, Meng L, Van Simaeys D, Chen H, Martin J, Tan W. Analyst. 2009; 134:1765–1775. [PubMed: 19684896]

241. Agnew HD, Rohde RD, Millward SW, Nag A, Yeo W-S, Hein JE, Pitram SM, Tariq AA, Burns VM, Krom RJ, Fokin VV, Sharpless KB, Heath JR. Angew. Chem. Int. Ed. 2009; 48:4944–4948.

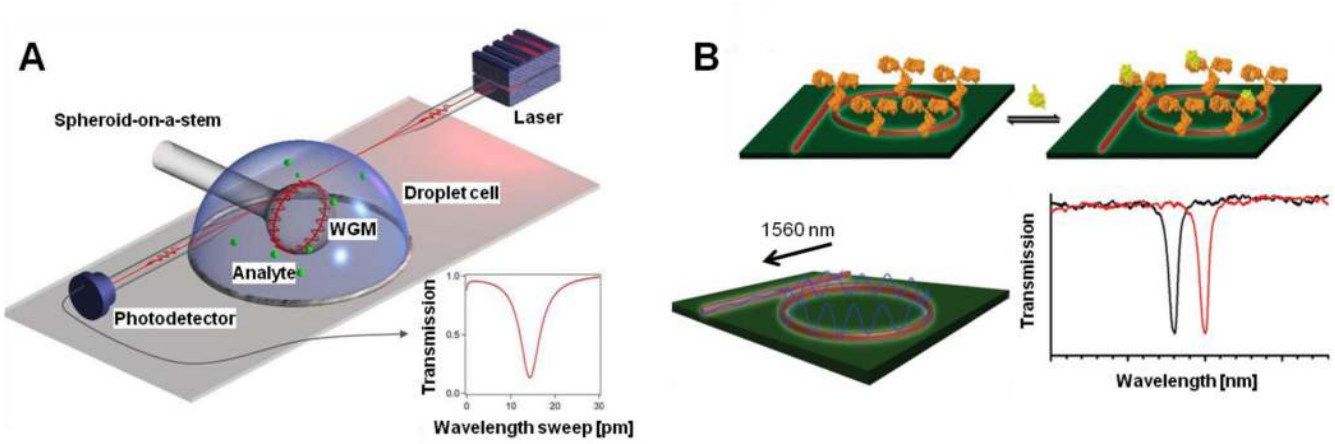

Figure 1.

Whispering gallery mode (WGM) sensing. (**A**) For a non-planar WGM microsphere geometry, light is coupled into a spheroid-on-a-stem structure from an adjacent, carefully aligned optical fiber. Light from a tunable laser propagates by total internal reflection through the fiber, and coupling to the microsphere occurs at resonant wavelengths (Equation 1). A photodetector records the resonance wavelength as a dip in the transmission spectrum. Adapted with permission from ref 56. © 2008 National Academy of Sciences, U.S.A. (**B**) Planar WGM microrings can be fabricated in silicon-on-insulator, allowing straightforward coupling form a linear waveguide to the ring. Interaction of molecules with a microring (in this case proteins binding to a capture antibody) causes a change in the local refractive index. When the resonance condition is met, light (~1560 nm) is coupled from the linear waveguide into the microring and constructively interferes to set up a standing wave. Attenuations in the transmission spectrum collected at the output of the linear waveguide coincide with the resonance wavelength. Changes in refractive index shift the resonance wavelength, as depicted by the shift from the black to red transmission spectrum. Adapted from ref 87. © 2009 American Chemical Society.

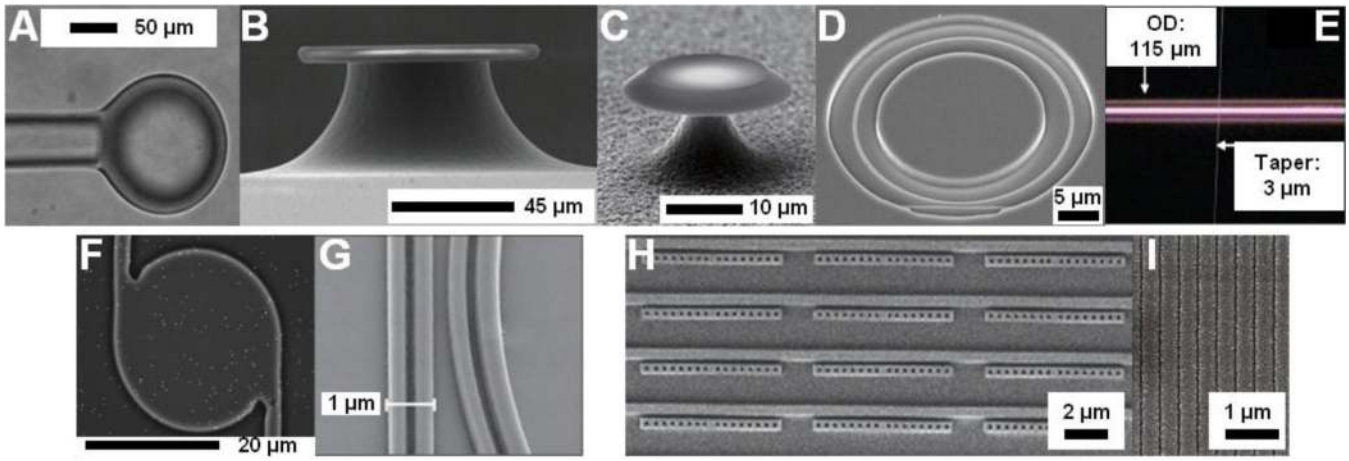

Figure 2.

High-Q geometries, as visualized by scanning electron microscopy. (**A**) Glass microsphere formed by heating a tapered optical fiber by Vollmer et al. Reproduced with permission from ref 56. © 2008 National Academy of Sciences, U.S.A. (**B**) Silica microtoroid fabricated by lithography, etching, and thermal reflow by Armani et al. Reproduced by permission from ref 42. © 2007 American Association for the Advancement of Science. (**C**) Silver-coated surface-plasmon-polariton WGM microdisk fabricated by Min et al. Reproduced by permission from ref 27. © 2009 Nature Publishing Group. (**D**) Silicon microring resonator inside lithographically defined annular opening in perfluoropolymer cladding by Luchansky et al. Reproduced by permission from ref 3. © 2010 Elsevier. (**E**) Liquid core optofluidic ring resonator fabricated from glass microcapillary by Zhu et al., with adjacent optical fiber taper for coupling. Adapted from ref 103. © 2007 American Chemical Society. (**F**) Hurricane microresonator device, showing association with gold nanoparticles by Koch et al. Reproduced by permission from ref 109. © 2010 Elsevier. (**G**) Coupling region of 140-µm slot microring resonator by Carlborg et al. Reproduced by permission from ref 98. © 2010 The Royal Society of Chemistry. (**H**) 1-D photonic crystals fabricated in silicon-on-oxide in a multiplexed geometry by Mandal et al. Reproduced by permission from ref 46. © 2009 The Royal Society of Chemistry. (**I**) Grating structure of TiO_2/SiO_2-coated replica-molded polymer photonic crystal by Huang et al. Adapted from ref 128. © 2011 American Chemical Society.

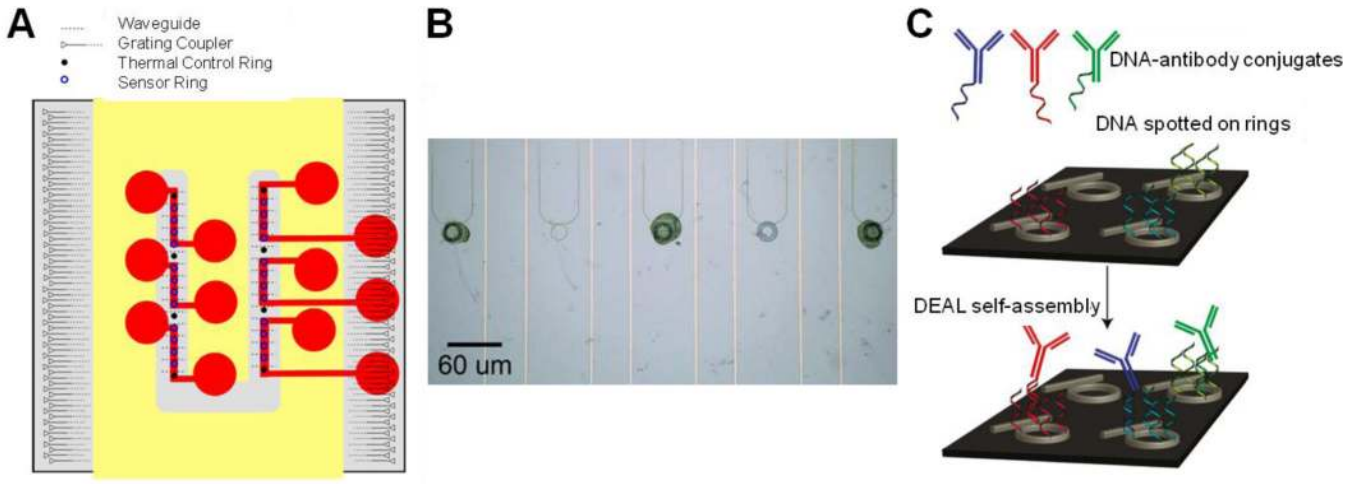

Figure 3.

Surface functionalization methods for microring arrays. (**A**) Use of 6-channel PDMS microfluidics for differential capture antibody functionalization of 6 groups of 4 microrings each. Adapted from ref 45. © 2010 American Chemical Society. (**B**) Non-contact piezoelectric (inkjet) method for spotting of air-stable glycans on individual microrings. Fluorescently labeled streptavidin alignment calibration is shown here. Reproduced by permission from ref 158. © 2011 The Royal Society of Chemistry. (**C**) One-step self-assembly of a DNA-encoded antibody library (DEAL) on individual DNA-functionalized microrings. DNA can be spotted robustly on microrings and retains functionality when dried, allowing subsequent direction of antibody loading. Adapted from ref 159. © 2011 American Chemical Society.

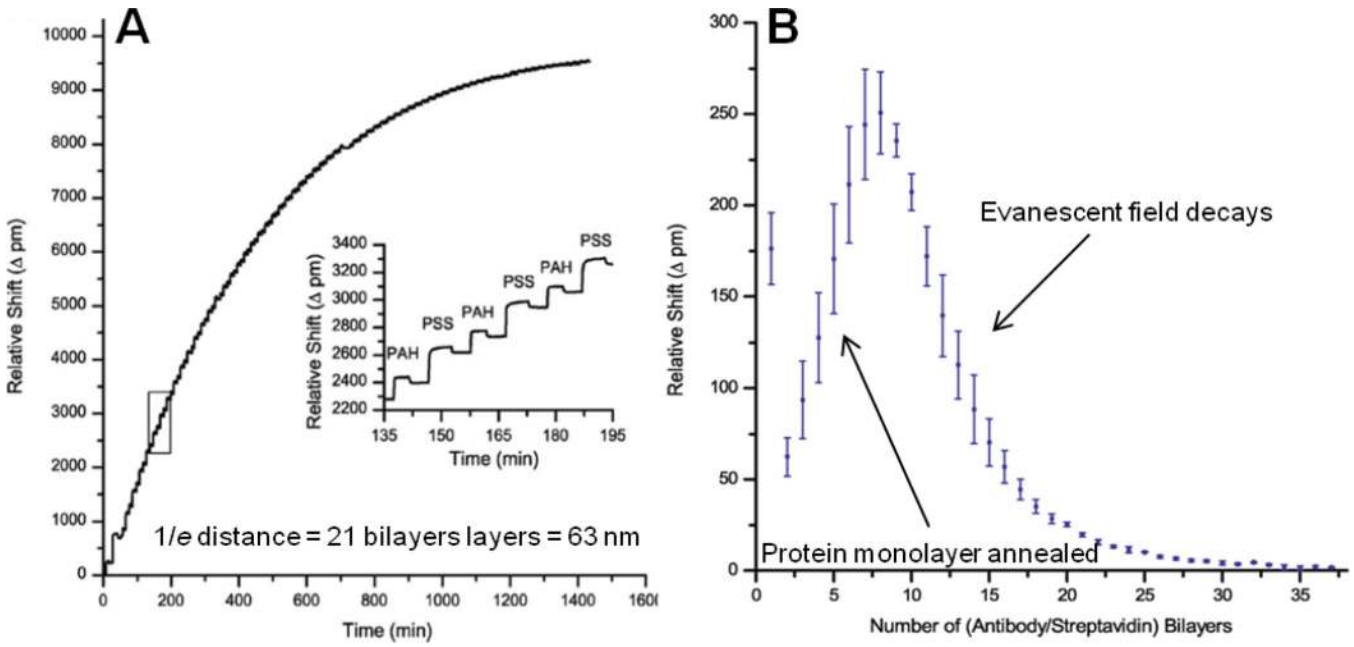

Figure 4.

Sensor characterization by evanescent field profiling. (**A**) Real-time plot showing the cumulative growth of 72 polyelectrolyte bilayers on a silicon microring. Inset shows sequential addition of 3 representative bilayers of polyallylamine HCl (PAH) and polystyrene sulfonate (PSS). The relative shift for each layer models the exponential decay of the evanescent field with increasing distance from the sensor surface, yielding a 1/*e* distance of 63 nm. (**B**) Protein multilayer growth plot displaying relative shift per biotin-antibody/streptavidin bilayer. After reaching a peak response of 250 pm at bilayer 8 as initial holes (incomplete surface coverage) of protein monolayer are annealed, subsequent layers show exponential signal decay as they are deposited farther from the ring surface. Error bars represent the standard deviation for *n*=4 rings. Reproduced by permission from ref 3. © 2010 Elsevier.

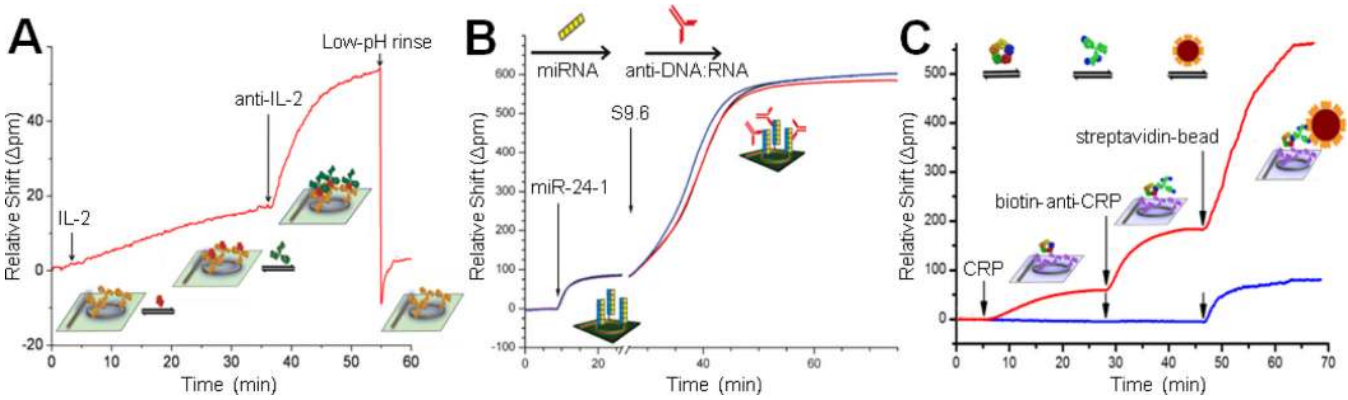

Figure 5.

Strategies for increased specificity and signal enhancement. (**A**) A sandwich immunoassay for the cytokine interleukin-2 (IL-2) utilizes a secondary antibody for added specificity and to amplify the primary signal. The surface can be regenerated with a low-pH rinse. Adapted from ref 145. © 2010 American Chemical Society. (**B**) Similarly, the use of a secondary antibody specific for the DNA:RNA heteroduplex (S9.6) amplifies the signal associated with miRNA 24-1 binding. Adapted from ref 137. © 2011 American Chemical Society. (**C**) A tertiary enhancement step can be used to amplify the signal further. In this case, streptavidin-conjugated 100-nm beads bind to a biotinylated secondary antibody in a three-step assay for the cardiac biomarker C-reactive protein (CRP). A low CRP concentration (blue curve) that was difficult to quantitate with a sandwich assay becomes easily observable with bead-based signal enhancement. Adapted by permission from ref 177. © 2011 The Royal Society of Chemistry.

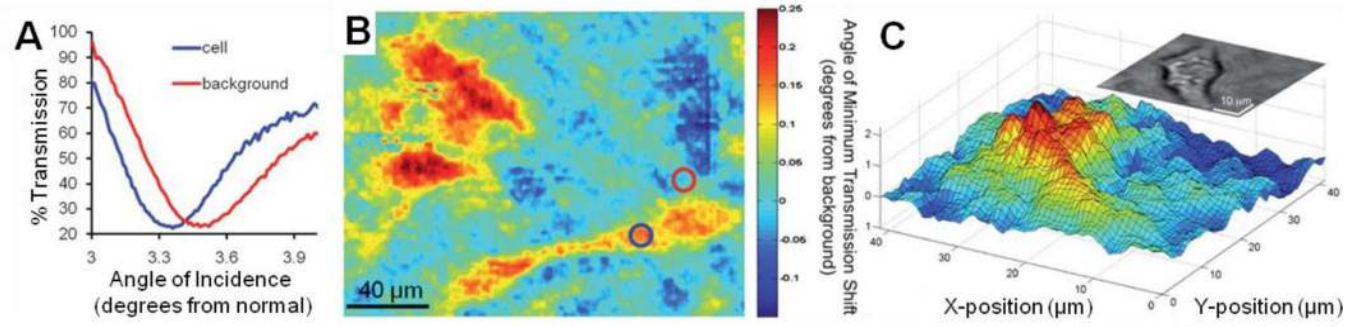

Figure 6.

Photonic crystal enhanced microscopy (PCEM) for cellular attachment imaging. (**A**) By illuminating a photonic crystal surface from below with a laser that is scanned through a range of incident angles, a transmission spectrum is obtained for each 0.61-μm^2 pixel to find the angle of minimum transmission (AMT). On-cell pixels have a reduced angle of minimum transmission relative to off-cell pixels. (**B**) Lidstone et al. use PCEM to image the attachment of hepatic carcinoma cells by mapping the AMT on a pixel-by-pixel basis with a CCD camera. (**C**) The morphology of cardiomyocte attachment visualized by a PCEM surface plot corresponds with optical microscopy observations (gray-scale inset). Adapted by permission from ref 198. © 2011 The Royal Society of Chemistry.

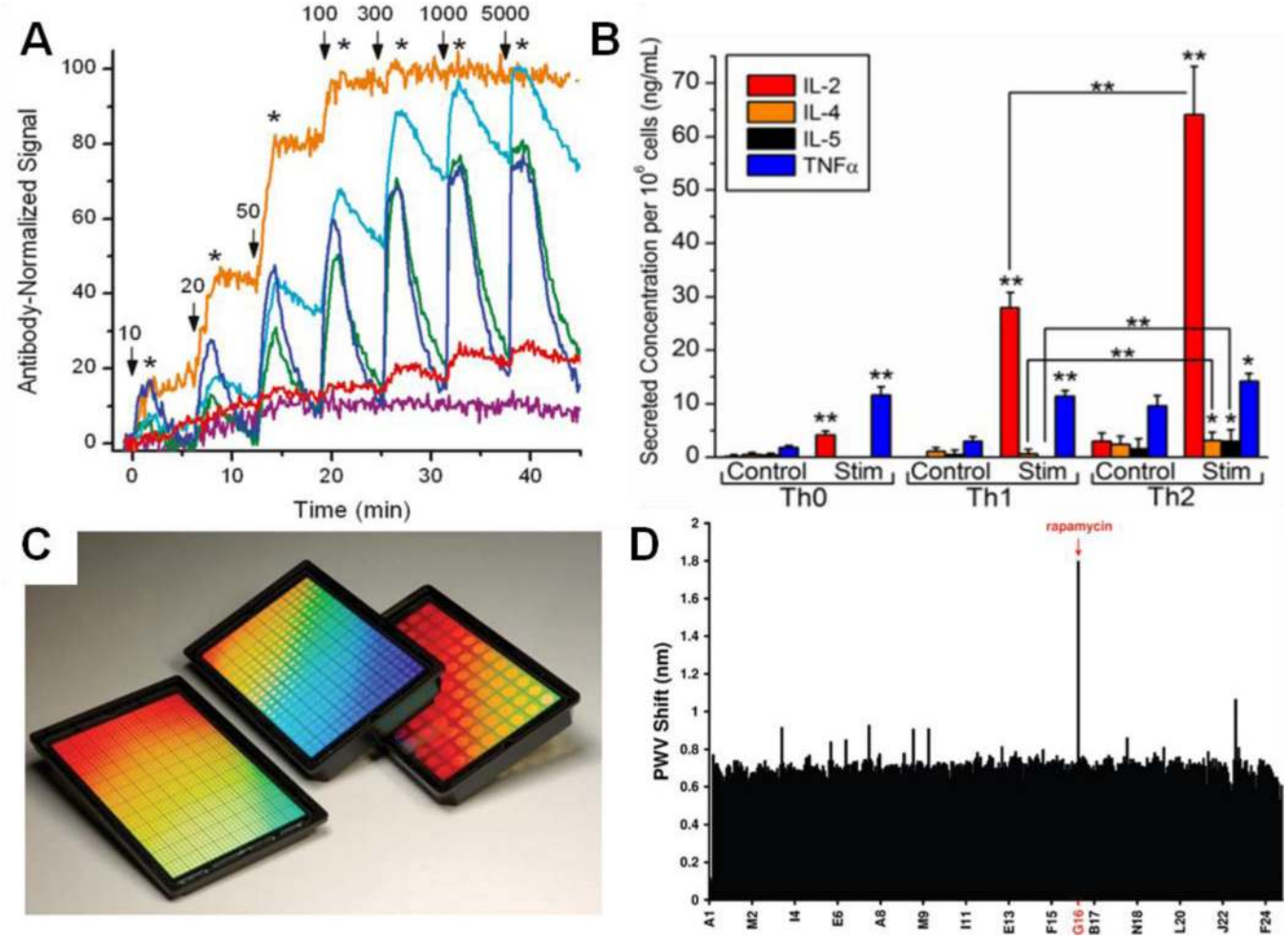

Figure 7.

Multiplexing applications of high-Q sensors. (**A**) DNA-encoded antibody libraries allow for rapid, parallel capture agent affinity profiling on a microring resonator array platform. In this case, 6 anti-prostate specific antigen (PSA) antibodies are screened in parallel with a kinetic titration (PSA concentrations, in ng/mL, noted above arrows) to allow rational selection of the best antibodies from multiple vendors. Real-time analysis allows for the calculation of association and dissociation rates. Adapted from ref 159. © 2011 American Chemical Society. (**B**) Microring resonator sensor arrays also allow for multiplexed cytokine profiling for T cell differentiation analysis. Normalized cytokine secretion levels for three differentiated primary T cell subsets (Th0, Th1, and Th2) were determined by one-step sandwich immunoassays. Control cultures on the left are compared to PMA/ionomycin-stimulated (Stim) cultures on the right, with a comparison of secretion levels by a paired difference *t*-test (*/** indicate significance at 95%/99%). Adapted from ref 157. © 2011 American Chemical Society. (**C**) These 96-, 384-, and 1536-well photonic crystal microplates permit high-throughput screening assays. Reproduced by permission from ref 17. © 2011 The Royal Society of Chemistry. (**D**) As an example of multiplexing applications of photonic crystal microplates, a 384-well high-throughput screen of protein-protein modulators correctly reveals rapamycin as necessary for FRB binding to immobilized FKBP12. Among the 320 compounds screened, a large peak wavelength value (PWV) only occurs in the presence of rapamycin. Reproduced by permission from ref 148. © 2009 American Chemical Society.

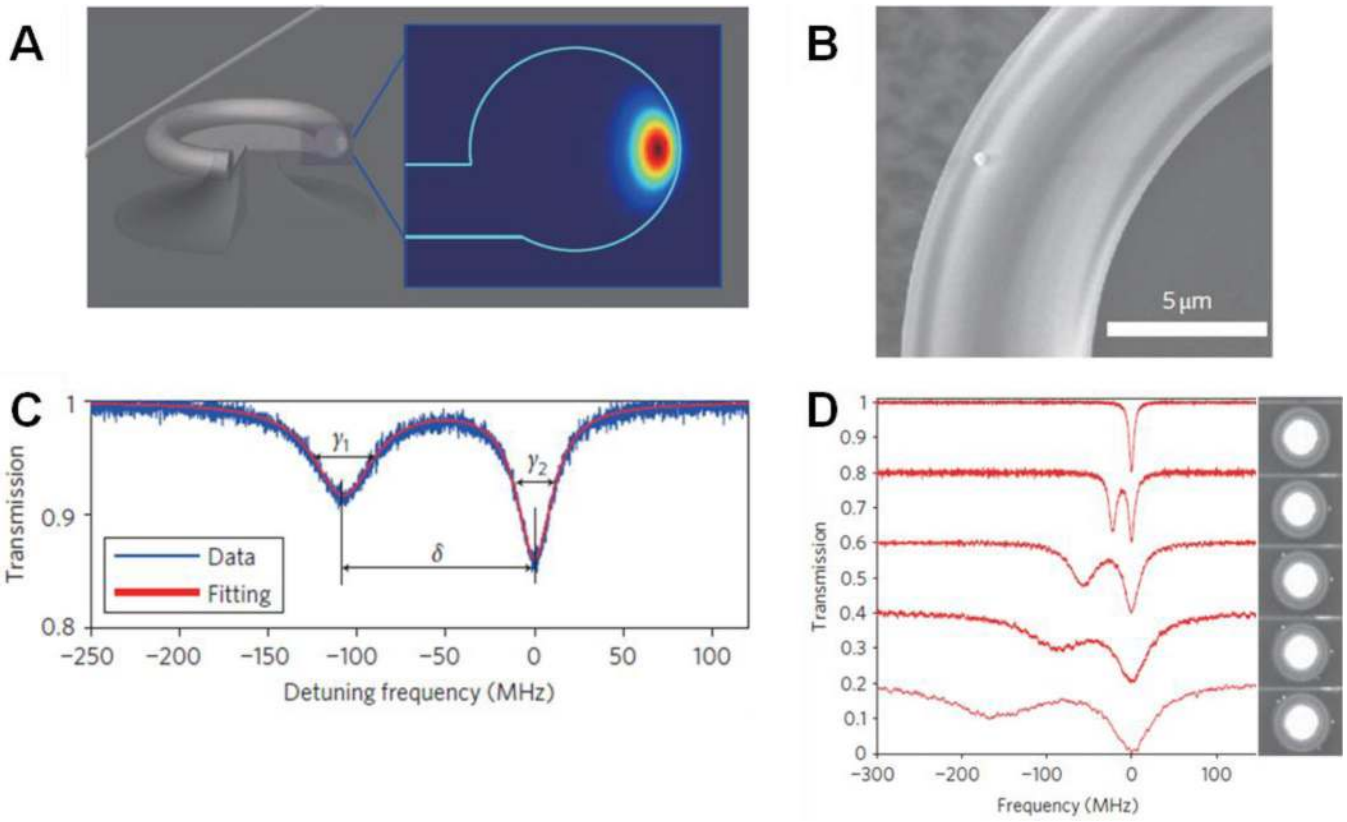

Figure 8.

Single nanoparticle detection and sizing. Zhu et al. utilize silicon microtoroids to detect and analyze single nanoparticles. (**A**) The fiber-coupled microtoroid and finite-element-method simulation of the WGM field profile in a toroidal cross-section are shown. (**B**) SEM allows for visualization of a 300-nm particle deposited on the high-Q resonator. Nanoparticle deposition causes scattering that breaks the symmetry in the microtoroid, lifting the degeneracy in the WGM modes that propagate in opposite directions in the toroid. (**C**) The resulting mode splitting doublet is the basis for single particle detection and sizing, and a representative transmission spectrum shows both symmetric (left) and asymmetric (right) modes. (**D**) Five transmission spectra show the splitting changes that accompany the deposition of successive KCl particles (zero to four particles, from top to bottom). Corresponding particle deposition images for particle counting are shown at the right. Reproduced by permission from ref 210. © 2010 Nature Publishing Group.

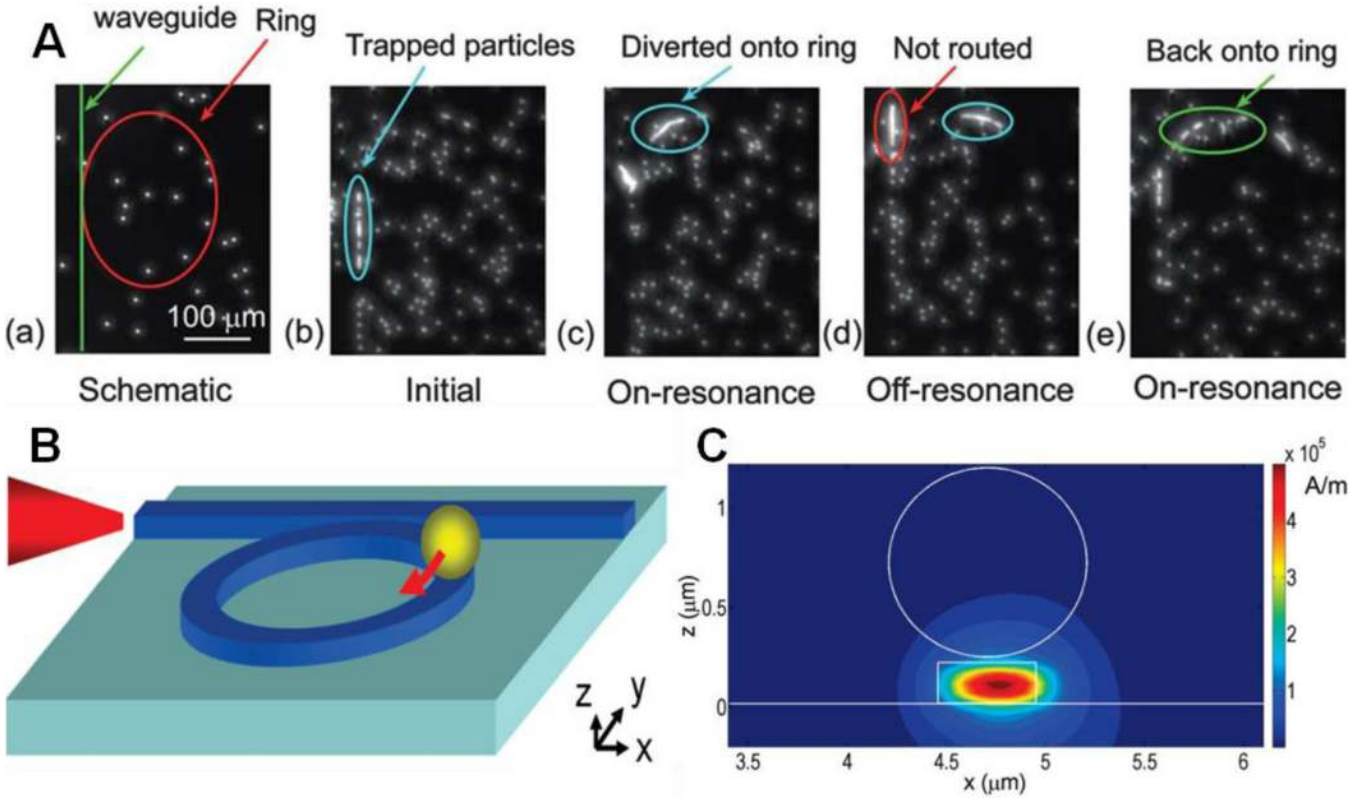

Figure 9.

Optical trapping and manipulation of particles. (**A**) CCD images of a racetrack microring and its adjacent bus waveguide (a) show the optical switching process for 3-μm polystyrene particles. (b) Initially, a string of particles is trapped on the bus waveguide. (c) The trapped particles are diverted to the microring at the resonance wavelength. Optical switching can be performed by moving from on-resonance to off-resonance wavelengths. (d) At off-resonance wavelengths, already-trapped particles remain on the ring, but the next group of particles is not diverted to the ring. (e) More particles can be diverted onto the ring upon return to the resonance wavelength. Reproduced by permission from ref 212. © 2010 The Royal Society of Chemistry. (**B**) Similar experiments by Lin et al. were used to trap polystyrene particles on much smaller (5–10-μm) microrings. Particle velocities and revolution frequencies were measured for trapped particles recirculating the microring. (**C**) The cross-section of a 10-μm microring and its accompanying WGM intensity below a trapped microsphere is shown. 3D-finite-difference time-domain (FDTD) simulations of electromagnetic field strength (in A/m) were performed at 1 W input power in the waveguide. The FDTD simulations show that the intensity on top of the ring follows a Gaussian distribution. Sections **B** and **C** reproduced by permission from ref 214. © 2010 American Chemical Society.

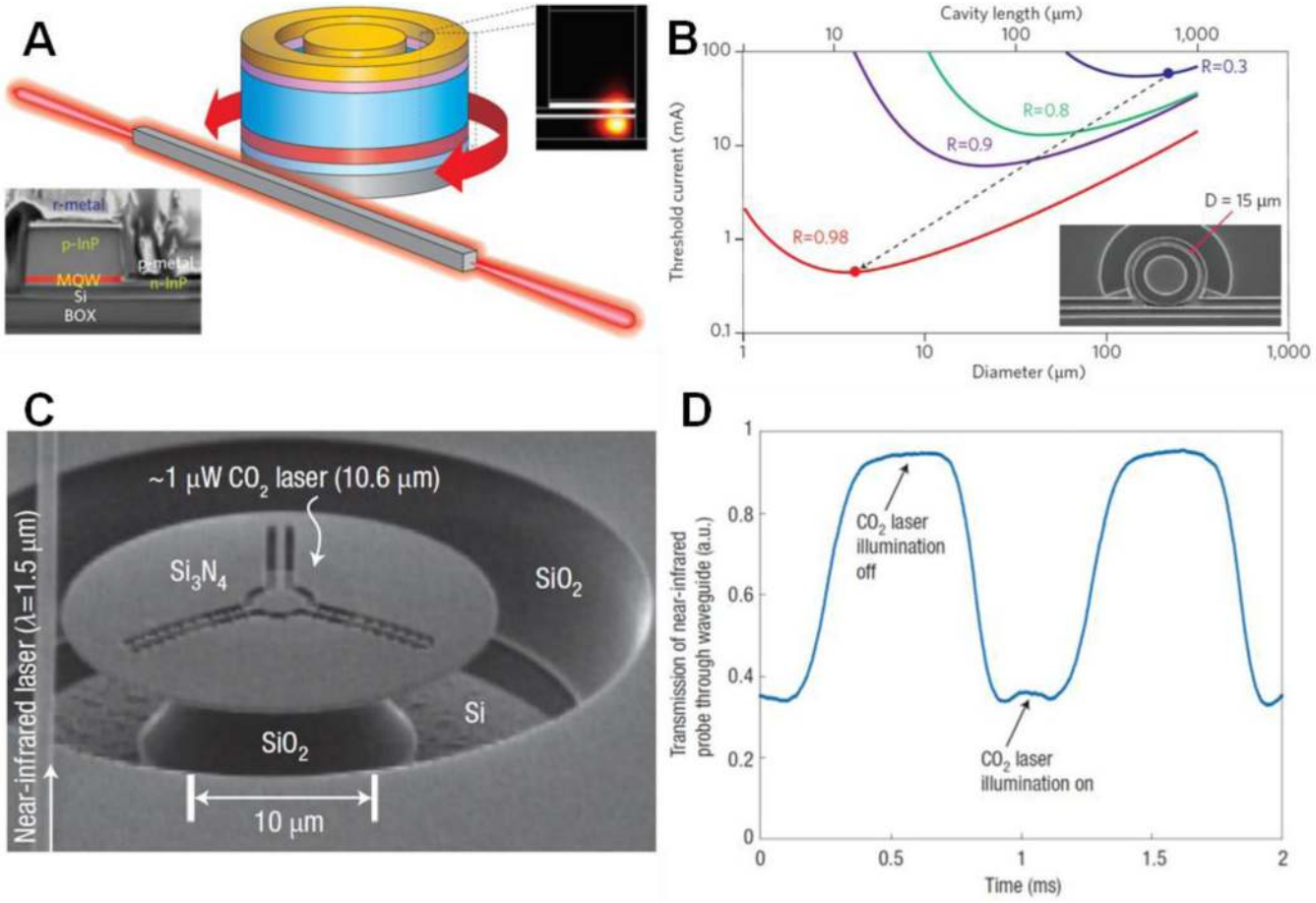

Figure 10.

Additional applications of high-Q devices: Compact silicon lasers and thermal imaging. (**A**) An electrically pumped microring resonator laser by Liang et al. is shown with an adjacent SOI bus waveguide, with the expanded view at right showing the fundamental transverse electrical mode localized toward the edge of the device. Stimulated emission is bidirectional. The inset at lower left is a cross-sectional SEM showing the metal layers and contacts. (**B**) Reduction of device diameter and improvements in facet reflectivity (R) will further reduce lasing thresholds, with 400 μA lasing threshold possible with a 4.5-μm device (red dot). The inset shows the top view of a 15-μm device. Sections **A** and **B** reproduced by permission from ref 227. © 2010 Nature Publishing Group. (**C**) Another interesting application of high-Q sensors is the creation of microphotonic thermal detectors. A representative silicon nitride resonator thermal detector device and adjacent waveguide is shown. (**D**) To demonstrate thermal sensitivity, the transmission through the adjacent waveguide is shown to vary with thermal fluctuations induced by a chopped CO_2 laser signal. Sections **C** and **D** reproduced by permission from ref 230. © 2007 Nature Publishing Group.